

Chapter 1

SPHINCS_BSSN: Numerical Relativity with Particles

Stephan Rosswog and Peter Diener

Abstract In this chapter we describe the *Lagrangian* numerical relativity code SPHINCS_BSSN. This code evolves spacetimes in full General Relativity by integrating the BSSN equations on structured meshes with a simple dynamical mesh refinement strategy. The fluid is evolved by means of freely moving Lagrangian particles, that are evolved using a modern Smooth Particle Hydrodynamics (SPH) formulation. To robustly and accurately capture shocks, our code uses artificial dissipation terms, but, similar to Finite Volume schemes, we apply a slope-limited reconstruction within the dissipative terms and we use in addition time-dependent dissipation parameters, so that dissipation is only applied where needed. The technically most complicated, but absolutely crucial part of the methodology, is the coupling between the particles and the mesh. For the mapping of the energy-momentum tensor $T_{\mu\nu}$ from the particles to the mesh, we use a sophisticated combination of "Local Regression Estimate" (LRE) method and a "multi-dimensional optimal order detection" (MOOD) approach which we describe in some detail. The mapping of the metric quantities from the grid to the particles is achieved by a quintic Hermite interpolation.

Apart from giving an introduction to our numerical methods, we demonstrate the accurate working of our code by presenting a set of representative relativistic hydrodynamics tests. We begin with a relativistic shock tube test, then compare the frequencies of a fully relativistic neutron star with reference values from the literature and, finally, we present full-blown merger simulations of irrotational binary

Stephan Rosswog (✉)

Sternwarte Hamburg, Gojenbergsweg 112, 21029 Hamburg, Germany & The Oskar Klein Centre, Department of Astronomy, Stockholm University, Stockholm, Sweden; e-mail: stephan.rosswog@uni-hamburg.de

Peter Diener

Center for Computation & Technology, Louisiana State University, 70803, Baton Rouge, LA, USA & Department of Physics & Astronomy, Louisiana State University, 70803, Baton Rouge, LA, USA e-mail: diener@cct.lsu.edu

systems, one case where a central remnant survives and another where a black hole forms, and of a binary where only one of the stars is rapidly spinning.

1.1 Introduction

Despite their early postulation by Albert Einstein in 1916 [1, 2], gravitational waves (GWs) remained a topic of sustained debate for more than half a century [3]. Their physical reality was only firmly established after the discovery of the Hulse-Taylor pulsar in 1974 [4]: the secular orbital decay of this neutron star binary system is in nearly perfect agreement with the prediction from Einstein’s theory and this finally brought the decades’ long controversy to an end. Still, the first *direct* detection of GWs had to wait until 2015 when both LIGO detectors recorded the last 0.2 seconds of the inspiral and the subsequent merger of two $\sim 30 M_{\odot}$ black holes [5].

The first detection of a GW source that actually involved *matter* (rather than “just black holes”), followed soon: in August 2017 a \sim minute-long GW-signal from a merging neutron star binary (GW170817) was detected. Most excitingly, this event was also observed in electromagnetic (EM) waves, first as a short gamma-ray burst (GRB) that followed the peak of the GW emission with a delay of 1.7 s, later (\sim days) as a radioactively powered thermal transient peaking at optical/near-infrared wavelengths frequently called a “kilonova”, and much later (\sim months) also in radio wavelengths, see [6] for a recent review.

This event meant a huge leap forward for many long-standing (astro-)physics questions. For example, the electromagnetic follow-up observations of GW170817 revealed the actual host galaxy where the merger took place and this placed the event in an astronomical environment and connected it to potential stellar evolution paths [7]. Since the distance to the host galaxy is known, it was possible to use the 1.7 s delay between GWs and the GRB to show that GWs propagate to a relative accuracy of 10^{-15} at the speed of light [8]. This, in turn, eliminated families of alternative theories of gravity where $c_{\text{GW}} \neq c$. GW170817 also demonstrated the exciting possibility to constrain the properties of cold nuclear matter via the effects of tidal deformability and thereby ruled out some very stiff equations of state [9]. The event further showed that neutron star mergers are, as expected on theoretical grounds [10, 11, 12, 13, 14], major cosmic production sites of heavy “r-process” elements [15], and that they are useful probes of the cosmic expansion [16].

All of these breakthroughs were enabled by the *combined* detection of the same event via different messengers, here GWs and photons. This detection splendidly illustrated the huge discovery potential of multi-messenger astrophysics, but it also underlined the enormous modelling challenge: in addition to strong-field gravity, relativistic fluid dynamics, neutrino transport, magnetic fields, nuclear reactions and atomic physics, also (non-equilibrium) radiative transfer should be included in theoretical models in order to make the connection to the EM observations.

Numerical simulations, especially numerical relativity simulations [17, 18, 19, 20], play a very crucial role in connecting the physical processes during merger to

potentially observable signals. Such simulations have increasingly become tools for exploring signatures from both established and more speculative parts of fundamental physics. Multi-physics numerical relativity simulations are extremely complex and time consuming: codes typically evolve several dozen variables per spacetime (grid-) point and, depending on the simulated physics, many more variables may be needed. For example, neutrino transport is needed to make detailed predictions for the neutron-to-proton-ratio in the ejecta, which, in turn, determines which elements are formed and therefore also how the electromagnetic signal looks like. But evolving several neutrino flavours, with many energy groups for each of them, becomes a serious extra computational burden [21, 22, 23]. To make things worse, the spacetime needs to be evolved with very small numerical time steps that are limited by the Courant criterion [24]. The "signal speed" that enters this criterion is the speed of light, which limits the admissible time steps to $\Delta t \approx 10^{-7} s \left(\frac{\Delta x}{100\text{m}} \right)$, where Δx is the spatial length to be resolved.

To date, essentially all numerical relativity codes that solve the full set of Einstein equations are *Eulerian*, i.e. they solve the fluid equations on computational (usually structured or adaptive) grids. The only exception is our code SPHINCS_BSSN [25, 26, 27, 28], which is the main topic of this book chapter. Using an alternative methodology makes it possible to independently cross-validate the longer established Eulerian methods, but it also comes with distinctive advantages for multi-messenger astrophysics. One of its salient features is that –contrary to Eulerian methods– vacuum does not need to be modelled hydrodynamically: it is simply characterized by the absence of computational elements (here: particles) and no computational resources need to be spent to evolve it. Moreover, the neutron star surface, which is an eternal source of numerical trouble for Eulerian methods, is very well-behaved and does not need any particular treatment compared to the rest of the fluid¹. The ejecta of a neutron star merger correspond to only $\sim 1\%$ of the binary mass, but they are responsible for essentially all of the EM emission. Therefore, the accurate prediction of the properties of this small amount of matter is of paramount importance for multi-messenger astrophysics. This is, in fact, one of the key strengths of a code like SPHINCS_BSSN: advection is exact (i.e. not depending on the resolution) and the properties of a particle, say its electron fraction Y_e , are simply transported by the particle unless they are changed by physical processes (e.g. by an electron capture reaction), but no purely numerical "diffusive" processes occur.

In the rest of this chapter, we will describe the methodology behind our Lagrangian Numerical Relativity code SPHINCS_BSSN and we will present some of the first applications. In Sec. 1.2 we will describe how we evolve fluids and, since in a numerical relativity context the use of particles is not widespread, we start with some basics of the SPH method. We further outline how the spacetime is evolved and how the fluid particles and the grid cells for the spacetime evolution exchange information. In Sec. 1.3 we will show some applications of the code including some

¹ This is illustrated later, see Fig. 1.6.

standard benchmark tests, but also some of the first astrophysical simulations. We finally will summarize this chapter in Sec. 1.4.

1.2 Methodology

Here we will briefly summarize the main methodological elements that enter in SPHINCS_BSSN. We will focus here on the main ideas and in some cases we will refer to our more technical papers [25, 26, 27, 28] for the full details.

1.2.1 Relativistic Smooth Particle Hydrodynamics

Our main aim here is to describe how we evolve matter by means of a modern, general relativistic Smooth Particle Hydrodynamics (SPH) code. But before we do so, we will summarize some basic SPH techniques and we will briefly discuss the (simpler to understand) Newtonian SPH approach. Once equipped with this basic knowledge, the general relativistic version should be straight forward to grasp.

This introduction to the topic is by no means meant as a comprehensive SPH review, for a more complete introduction to the SPH-method, its variants and subtleties and its various applications in astrophysics and cosmology, we refer to extensive reviews that exist in the literature [29, 30, 31, 32, 33, 34, 35]. For relativistic formulations of SPH, we specifically want to point to [36, 37, 38, 31, 39, 40, 41, 25, 26, 27, 28]. Among these, we will frequently refer to [31] since here many results are derived very explicitly in a step-by-step fashion.

1.2.1.1 A primer on basic SPH-techniques

The main idea of SPH is to model a fluid via spherical particles of finite size and overlapping support. These particles move with the local fluid velocity, i.e. SPH is a fully *Lagrangian* method, as opposed to Eulerian or Adaptive Lagrangian Eulerian, or "ALE", methodologies. The overlapping nature of the particles distinguishes them, for example, from (usually quasi-) Lagrangian Moving Mesh methods, see e.g. [42, 43], which instead tessellate space into non-overlapping cells which have a sharp interface surface between them. The task is now to translate the continuum equations of Lagrangian fluid dynamics into evolution equations for the particles, ideally in a way that ensures that nature's conservation laws are enforced on the level of the particle evolution equations. In the simplest case of ideal, non-relativistic fluids the equations read

$$\frac{d\rho}{dt} = -\rho \nabla \cdot \vec{v} \quad (1.1)$$

$$\frac{d\vec{v}}{dt} = -\frac{\nabla P}{\rho} + \vec{f} \quad (1.2)$$

$$\frac{du}{dt} = \frac{dq}{dt} + \frac{P}{\rho^2} \frac{d\rho}{dt}. \quad (1.3)$$

Here, ρ is the mass density, \vec{v} the fluid velocity, P the pressure, \vec{f} denote other "body forces" e.g. from gravity, u is the specific internal energy (i.e. energy per mass) and dq/dt denotes potential sources of heating and/or cooling. The Lagrangian time derivative, d/dt , is related to the Eulerian time derivative $\partial/\partial t$ by

$$\frac{d}{dt}(\cdot) = \left(\frac{\partial}{\partial t} + \vec{v} \cdot \nabla \right) (\cdot). \quad (1.4)$$

Note that Eq. (1.3) is simply the first law of thermodynamics written "on a per mass basis", i.e. the involved quantities are e.g. energy per mass or volume per mass (=1/density).

At the heart of the SPH method is kernel interpolation. Assuming that some quantity f is known at particle location b , a smoothed version of the quantity $\langle f \rangle$ reads

$$\langle f \rangle(\vec{r}) = \int f(\vec{r}') W_h(\vec{r}' - \vec{r}) d^3 x' \approx \sum_b V_b f_b W_h(\vec{r}_b - \vec{r}) = \sum_b \frac{m_b}{\rho_b} f_b W_h(\vec{r}_b - \vec{r}). \quad (1.5)$$

Here W_h is a smoothing kernel, see below, whose support size is determined by the length scale h , which, in an SPH context, is usually referred to as the "smoothing length". In the approximation we have applied a one-point quadrature. In SPH, one usually chooses the particle volume as m_b/ρ_b , where m_b and ρ_b are the particle mass and mass density at the position of particle b , but other choices are possible, see e.g. [44, 34, 45] for alternatives. One simple application of Eq. (1.5) is to choose the density ρ for the quantity f , which yields

$$\langle \rho \rangle_a = \sum_b m_b W_{ab}(h_a), \quad (1.6)$$

where $W_{ab}(h_a)$ is a short-hand for $W((\vec{r}_a - \vec{r}_b)/h_a)$. In other words: the density can be calculated by summing over the local neighbourhood and weighting each particle's mass according to how far away it is from particle a . If one keeps each particle's mass fixed in time, one has enforced *exact* mass conservation and one does not have to solve the mass conservation equation (1.1) explicitly, but one can do so if this is desired.

Clearly, for the smoothing procedure in Eq. (1.5) to make sense, the smoothing kernel must have certain properties:

- it needs to be normalized, $\int W_h(\vec{r}') d^3 r' = 1$,
- obviously, the dimension of the kernel has to be "1/volume",

- it has to have the “delta-property”, so as to reproduce the original function in the limit of vanishing support size,

$$\lim_{h \rightarrow 0} \int W_h(\vec{r}' - \vec{r}) f(r') d^3 r' = f(r) \quad (1.7)$$

- and it should (at least) have a continuous second derivative.

A number of other properties are desirable, for example, the kernel should be “radial”, i.e. $W_h(\vec{x} - \vec{x}') = W_h(|\vec{x} - \vec{x}'|)$, to easily allow for the conservation of momentum and angular momentum, and its Fourier transform should fall off rapidly with wave number [46]. As a side remark: it may seem appealing to use an oblate kernel to model, say, an accretion disk, but this approach would sacrifice one of SPH’s most salient features: its exact angular momentum conservation. The latter can be easily enforced when radial kernel are used, see Sec. 2.4 in [31] for an explicit demonstration how radial kernels lead to exact angular momentum conservation.

For a gradient estimate, one can straight forwardly apply the nabla operator to Eq. (1.5)²

$$\nabla f(\vec{r}) = \sum_b \frac{m_b}{\rho_b} f_b \nabla_r W_h(\vec{r}_b - \vec{r}), \quad (1.8)$$

where the index r at the nabla operator indicates that the derivative is taken with respect to the variable \vec{r} (rather than \vec{r}_b). The derivatives are usually needed at the position of a particle (here labelled a) and abbreviated as

$$(\nabla f)_a = \sum_b \frac{m_b}{\rho_b} f_b \nabla_a W_{ab}(h_a), \quad (1.9)$$

where the label at the nabla operator is again a reminder that the derivative is taken with respect to \vec{r}_a (and not \vec{r}_b). From Eq. (1.5) it is obvious that one would want to have the “partition of unity” property in a discrete form at any position \vec{r}

$$1 = \sum_b \frac{m_b}{\rho_b} W_h(\vec{r}_b - \vec{r}) \quad (1.10)$$

$$0 = \nabla_r(1) = \sum_b \frac{m_b}{\rho_b} \nabla_r W_h(\vec{r}_b - \vec{r}), \quad (1.11)$$

where the second equation is simply the result of applying the nabla operator to the first one. In standard SPH these equations are only approximately fulfilled and the accuracy depends on the kernel function used, its support size (or the number of contributing particles) and on the exact particle distribution. This has the effect, that when applying Eq. (1.8) to a constant function $f = f_0$, one only approximately recovers the theoretical value of zero

$$\nabla_r \left(\sum_b \frac{m_b}{\rho_b} f_b W_h(\vec{r}_b - \vec{r}) \right) = f_0 \sum_b \frac{m_b}{\rho_b} \nabla_r W_h(\vec{r}_b - \vec{r}) \approx 0. \quad (1.12)$$

² From now on we drop the distinction between a function and its numerical approximation.

This, however, can be easily corrected by simply “subtracting a numerical zero”, so that a better gradient estimate reads

$$\begin{aligned} (\nabla f)_a^{(1)} &= \sum_b \frac{m_b}{\rho_b} f_b \nabla_a W_{ab}(h_a) - \left(f_a \sum_b \frac{m_b}{\rho_b} \nabla_a W_{ab}(h_a) \right) \\ &= \sum_b \frac{m_b}{\rho_b} (f_b - f_a) \nabla_a W_{ab}(h_a), \end{aligned} \quad (1.13)$$

and this expression vanishes by construction when all f_k are the same. As an example, we can apply this gradient prescription to find an estimate for the velocity divergence. This quantity plays an important role in fluid dynamics, since $\nabla \cdot \vec{v} = 0$ defines “incompressibility”, while $\nabla \cdot \vec{v} > 0$ indicates local expansion and $\nabla \cdot \vec{v} < 0$ means local compression of the fluid. The resulting expression is

$$(\nabla \cdot \vec{v})_a = \sum_b \frac{m_b}{\rho_b} (\vec{v}_b - \vec{v}_a) \cdot \nabla_a W_{ab}(h_a). \quad (1.14)$$

An alternative discretization can be found by taking Eq. (1.1) and calculating the Lagrangian time derivative of Eq. (1.6) directly

$$(\nabla \cdot \vec{v})_a = -\frac{1}{\rho_a} \frac{d\rho_a}{dt} = -\frac{1}{\rho_a} \sum_b m_b \frac{dW_{ab}}{dt} = \frac{1}{\rho_a} \sum_b m_b (\vec{v}_b - \vec{v}_a) \cdot \nabla_a W_{ab}(h_a), \quad (1.15)$$

where we have taken the straight-forward Lagrangian time derivative of the kernel function (see the kernel table in Sec. 2.3 in [31] where this is shown explicitly). Thus, we have derived an alternative numerical discretization for $\nabla \cdot \vec{v}$, where the difference between the two estimates is whether the local density (“ ρ_a ”) or the weighted nearby densities (“ ρ_b ”) are used. Both are equally valid and both vanish for the uniform velocity case.

For easy later reference, we explicitly write down once more the Lagrangian time derivative of the density in Eq. (1.6) that we have just found

$$\frac{d\rho_a}{dt} = \sum_b m_b \frac{d}{dt} [W_{ab}(h_a)] = \sum_b m_b (\vec{v}_a - \vec{v}_b) \cdot \nabla_a W_{ab}(h_a) \quad (1.16)$$

and we also note that

$$\nabla_a \rho_b = \sum_k m_k \nabla_a W_{bk}(h_b) \quad (1.17)$$

(the detailed steps can be found in Sec. 3.2 of [31]). Note that we have neglected small terms, usually called “grad-h” terms, that result from taking derivatives of the kernel with respect to the smoothing lengths. These terms have been derived for Newtonian hydrodynamics by [47, 48], for special-relativistic SPH in [40] and for the General Relativistic case in [39]. We had explored the effects of these grad-h terms in [49], but found them to be too close to unity to warrant the extra effort of an additional iteration (ρ depends on h and h depends on ρ , so one needs an iteration

for consistent values). Therefore, we will ignore these "grad-h"-terms for the rest of this chapter.

1.2.1.2 Newtonian SPH

We have already seen in Eq. (1.6) that the continuity equation does not need to be solved explicitly, and if we keep the particle masses fixed, we have enforced exact mass conservation. It now turns out that by insightful choices (see the discussion in Sec. 2.3 - 2.5 in [31]), one can also bring the energy and momentum equation into discrete forms so that they conserve the total energy and momentum exactly. If a radial kernel is used, then the total angular momentum is conserved exactly by construction³ as well. Keep in mind that this exact conservation even holds at finite resolution, which is not the case for Eulerian methods. Moving-mesh methods, see e.g. [42, 43], usually show good overall conservation, but angular momentum is not conserved exactly.

One can, however, also achieve exact conservation in a more elegant way: by starting from a Lagrangian and by applying a variational principle [50, 51, 38, 47, 31, 33] one finds a fully conservative discrete form of the equations without ambiguities.

As before, we will start here with the simplest case of ideal, Newtonian hydrodynamics, but one can adhere to this strategy also for cases with additional physics, e.g. gravity [52]. One can start from a discretized Lagrangian of an ideal fluid

$$L = \sum_b m_b \left(\frac{v_b^2}{2} - u_b \right) \quad (1.18)$$

and apply the Euler-Lagrange equations

$$\frac{d}{dt} \frac{\partial L}{\partial \vec{v}_a} - \frac{\partial L}{\partial \vec{r}_a} = 0 \quad (1.19)$$

to find the momentum evolution equation of each particle, where $\partial L / \partial \vec{v}_a$ is the canonical momentum, which for Eq. (1.18) simply becomes $m_a \vec{v}_a$. We can use again fixed particle masses and the adiabatic first law of thermodynamics, $du = -Pd(1/\rho)$, which yields

$$\left(\frac{\partial u}{\partial \rho} \right)_s = \frac{P}{\rho^2}, \quad (1.20)$$

where s denotes the specific entropy. This yields

³ This statement assumes that forces and time integration have a zero/negligible error. Obviously, time integration or approximate forces, e.g. from a gravity solver, can in practice introduce violations of *exact* conservation.

$$\begin{aligned} \frac{d\vec{v}_a}{dt} &= \frac{1}{m_a} \frac{\partial L}{\partial \vec{r}_a} = -\frac{1}{m_a} \sum_b m_b \frac{\partial u_b}{\partial \rho_b} \frac{\partial \rho_b}{\partial \vec{r}_a} = -\frac{1}{m_a} \sum_b m_b \frac{P_b}{\rho_b^2} \left[\sum_k m_k \nabla_a W_{bk}(h_b) \right] \\ &= -\sum_b m_b \left(\frac{P_a}{\rho_a^2} \nabla_a W_{ab}(h_a) + \frac{P_b}{\rho_b^2} \nabla_a W_{ab}(h_b) \right), \end{aligned} \quad (1.21)$$

where we have used $\nabla_a W_{bk} = \nabla_b W_{kb}(\delta_{ba} - \delta_{ka})$, see Sec. 2.3 in [31]. For the energy equation, a straight forward insertion of Eq. (1.15) into Eq. (1.3) (without the heating/cooling term) yields

$$\frac{du_a}{dt} = \frac{P_a}{\rho_a^2} \sum_b m_b (\vec{v}_b - \vec{v}_a) \nabla_a W_{ab}(h_a), \quad (1.22)$$

and with Eqs. (1.6), (1.21) and (1.22) we now have a complete set of discrete hydrodynamics equations. For practical simulations one would still need to choose an equation of state so that one can calculate pressures and one has to add dissipative mechanisms, e.g. a Riemann solver or artificial viscosity, so that shocks can be handled robustly.

1.2.1.3 General relativistic SPH

Special- and general-relativistic versions of SPH can be derived similarly to the Newtonian case [38, 31, 40, 39]. We use geometric units with $G = c = 1$ and adopt $(-, +, +, +)$ for the metric signature of the metric. We reserve greek letters for space-time indices from 0...3 with 0 being the temporal component and we use i and j for spatial components and SPH particles are labeled by a, b and k . Contravariant spatial indices of a vector quantity \vec{V} at particle a are denoted as V_a^i , while covariant ones will be written as $(V_i)_a$. The line element and proper time are given by $ds^2 = g_{\mu\nu} dx^\mu dx^\nu$ and $d\tau^2 = -ds^2$ and the proper time is related to the coordinate time t by

$$\Theta d\tau = dt, \quad (1.23)$$

where we have introduced a generalization of the Lorentz-factor

$$\Theta \equiv \frac{1}{\sqrt{-g_{\mu\nu} v^\mu v^\nu}}. \quad (1.24)$$

The coordinate velocity components are given by

$$v^\mu = \frac{dx^\mu}{dt} = \frac{dx^\mu}{d\tau} \frac{d\tau}{dt} = \frac{U^\mu}{\Theta} = \frac{U^\mu}{U^0}, \quad (1.25)$$

where we have used Eq. (1.23) and U^μ is the four-velocity which is normalized,

$$U^\mu U_\mu = -1. \quad (1.26)$$

The Lagrangian of a relativistic fluid is given by [53]

$$L = - \int T^{\mu\nu} U_\mu U_\nu \sqrt{-g} dV, \quad (1.27)$$

where $g = \det(g_{\mu\nu})$ and $T^{\mu\nu}$ denotes the energy-momentum tensor which, for an ideal fluid, reads

$$T^{\mu\nu} = (\tilde{\rho} + P) U^\mu U^\nu + P g^{\mu\nu}. \quad (1.28)$$

Here $\tilde{\rho}$ is the energy density measured in the local rest frame of the fluid and P is its pressure. For clarity, we will write out explicit factors of c in the following lines. The energy density possesses a contribution from the rest mass and one from the thermal energy:

$$\tilde{\rho} = \rho + u\rho/c^2 = nm_0c^2(1 + u/c^2). \quad (1.29)$$

Here n is the baryon number density in the local fluid rest frame, m_0 is the baryon mass and $u = u(n, s)$ the specific energy, with s being the specific entropy.⁴ In SPHINCS_BSSN we measure all energies in units of m_0c^2 . With this convention (and now using again $c = 1$) the energy momentum tensor reads

$$T^{\mu\nu} = \{n(1 + u) + P\} U^\mu U^\nu + P g^{\mu\nu}. \quad (1.30)$$

To perform practical simulations, we give up general covariance and choose a particular frame ('computing frame') in which the simulations are performed. Like in special-relativistic hydrodynamics, one must clearly distinguish between quantities that are measured in the computing frame and those measured in the local rest frame of the fluid. With the normalization of the four-velocity, Eq. (1.26), the Lagrangian can be written as

$$L = - \int n(1 + u) \sqrt{-g} dV. \quad (1.31)$$

Local baryon number conservation, $(U^\mu n)_{;\mu} = 0$, can be expressed as

$$\frac{1}{\sqrt{-g}} \partial_\mu (\sqrt{-g} U^\mu n) = 0, \quad (1.32)$$

where we have used an identity for the covariant derivative [54]. More explicitly, we can write

$$\partial_i(N) + \partial_i(Nv^i) = 0, \quad (1.33)$$

where we have made use of Eq. (1.25) and have introduced the computing frame baryon number density

$$N = \sqrt{-g} \Theta n. \quad (1.34)$$

In the special relativistic limit $g_{\mu\nu} \rightarrow \eta_{\mu\nu}$ (Minkowski), Θ reduces to the special relativistic Lorentz factor γ and $\sqrt{-g}$ becomes unity. In this limit, the computing

⁴ Here we simply use $m_0 = m_u$ for the average baryon mass, where m_u is the atomic mass unit. In reality, m_0 depends on the exact composition, but even in extreme cases the deviations from m_u are only a small fraction of a percent. See Sec. 2.1 in [26] for a more detailed discussion.

frame density N_{sr} is equal to the local rest frame density n multiplied by the Lorentz factor γ between the fluid rest frame and the computing frame. This, of course, makes perfect sense: think of a box in the rest frame of the fluid that contains a certain number of baryons. If this box moves with respect to the computing frame along a coordinate axis, the corresponding box edge appears Lorentz contracted in the computing frame, so that an observer in the computing frame would conclude that the density is

$$N_{\text{sr}} = \gamma n. \quad (1.35)$$

The total conserved baryon number, \mathcal{N} , can then be expressed as a sum over fluid parcels with volume ΔV_b located at \vec{r}_b , where each parcel carries a baryon number⁵ v_b

$$\mathcal{N} = \int N dV \simeq \sum_b N_b \Delta V_b = \sum_b v_b, \quad (1.36)$$

therefore the particle volume in the computing frame reads $\Delta V_b = v_b/N_b$. Eq. (1.33) looks like the Newtonian continuity equation and we will use it for the SPH discretization process. Similar to Eq. (1.5), a quantity f can now be approximated by

$$\langle f \rangle(\vec{r}) \simeq \sum_b \frac{v_b}{N_b} f_b W(\vec{r} - \vec{r}_b, h), \quad (1.37)$$

where the particle's baryon number v_b replaces the mass and the Newtonian mass density ρ is replaced by the computing frame baryon number density N . The latter can be calculated, very similarly to the Newtonian case, as

$$N_a = \sum_b v_b W_{ab}(h_a). \quad (1.38)$$

If each particle keeps its baryon number constant, we have exact baryon number conservation. The fluid Lagrangian, Eq. (1.31), then becomes

$$L = - \int \frac{1+u}{\Theta} N dV \approx - \sum_b \left(\frac{1+u}{\Theta} \right)_b N_b \Delta V_b = - \sum_b v_b \left(\frac{1+u}{\Theta} \right)_b, \quad (1.39)$$

where in the last step we have made use of the volume element $\Delta V_b = v_b/N_b$, as suggested by Eq. (1.36).

Again, as in the Newtonian case, one can use the Euler-Lagrange equations

$$\frac{d}{dt} \frac{\partial L}{\partial v_a^i} - \frac{\partial L}{\partial x_a^i} = 0, \quad (1.40)$$

to derive an evolution equation for the canonical momentum. One can use the Lagrangian to define a canonical momentum

⁵ Be careful not to confuse the baryon number v_b with the velocity component of a particle v_b^i .

$$(p_i)_a \equiv \frac{\partial L}{\partial v_a^i} = -\frac{\partial}{\partial v_a^i} \sum_b v_b \left(\frac{1+u}{\Theta} \right)_b. \quad (1.41)$$

Note that here $\partial u_b / \partial v_a^i$ has a non-zero value, since

$$\frac{\partial u_b}{\partial v_a^i} = \frac{\partial u_b}{\partial n_b} \frac{\partial n_b}{\partial v_a^i} = \frac{P_b}{n_b^2} \frac{\partial}{\partial v_a^i} \left(\frac{N_b}{\sqrt{-g} \Theta_b} \right), \quad (1.42)$$

where we have used the first law of thermodynamics and the relation Eq. (1.34) and the velocity dependence comes in via Θ , see Eq. (1.24) and one finds [39]

$$\frac{\partial}{\partial v_a^i} \left(\frac{1}{\Theta_b} \right) = -\Theta_b (g_{i\mu} v^\mu)_a \delta_{ab}. \quad (1.43)$$

The *canonical momentum per baryon* reads

$$(S_i)_a \equiv \frac{1}{v_a} \frac{\partial L}{\partial v_a^i} = \Theta_a \left(1 + u_a + \frac{P_a}{n_a} \right) (g_{i\mu} v^\mu)_a = \left(1 + u_a + \frac{P_a}{n_a} \right) (U_i)_a. \quad (1.44)$$

Similarly, one can use the canonical energy

$$E \equiv \sum_a \frac{\partial L}{\partial v_a^i} v_a^i - L = \sum_a v_a \left(v_a^i (S_i)_a + \frac{1+u_a}{\Theta_a} \right) \quad (1.45)$$

to identify the *canonical energy per baryon*

$$e_a \equiv v_a^i (S_i)_a + \frac{1+u_a}{\Theta_a}. \quad (1.46)$$

The evolution equation for the canonical momentum per baryon follows, according to the Euler-Lagrange equations (1.40), from $\frac{d(S_i)_a}{dt} = \frac{1}{v_a} \frac{\partial L}{\partial x_a^i}$, and after some algebra [39] one finds⁶

$$\frac{d(S_i)_a}{dt} = -\sum_b v_b \left\{ \frac{P_a}{N_a^2} D_i^a + \frac{P_b}{N_b^2} D_i^b \right\} + \left(\frac{\sqrt{-g}}{2N} T^{\mu\nu} \frac{\partial g_{\mu\nu}}{\partial x^i} \right)_a, \quad (1.47)$$

where we have introduced the abbreviations

$$D_i^a \equiv \sqrt{-g_a} \frac{\partial W_{ab}(h_a)}{\partial x_a^i} \quad \text{and} \quad D_i^b \equiv \sqrt{-g_b} \frac{\partial W_{ab}(h_b)}{\partial x_a^i}. \quad (1.48)$$

The first term in Eq. (1.47) (including the summation) is due to hydrodynamic accelerations and it is formally very similar to the Newtonian momentum equation (1.21), although the involved quantities have a different meaning. The second term represents the metric accelerations from the spacetime curvature and it depends on

⁶ Note that here we are omitting the "grad-h terms", see [39] for the explicit expressions including these small correction terms.

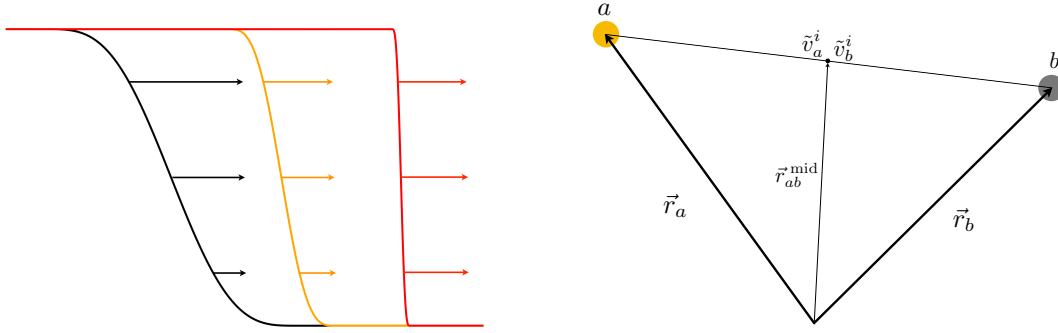


Fig. 1.1: Left: sound wave steepening into a shock. Right: reconstruction of the particle velocities to the mid-point between two particles.

the spatial derivatives and the determinant of the metric.

The evolution equation of canonical energy per baryon follows from straight forwardly taking the Lagrangian time derivative of Eq. (1.46), applying the first law of thermodynamics and after some algebra [39] one obtains

$$\frac{de_a}{dt} = - \sum_b v_b \left\{ \frac{P_a v_b^i}{N_a^2} D_i^a + \frac{P_b v_a^i}{N_b^2} D_i^b \right\} - \left(\frac{\sqrt{-g}}{2N} T^{\mu\nu} \partial_t g_{\mu\nu} \right)_a. \quad (1.49)$$

Similar to the momentum equation, there is a hydrodynamic contribution (involving the summation over neighbour particles) and a gravitational contribution that is proportional to the time derivative of the metric tensor.

The attentive reader may wonder how one finds the physical variables (i.e. v^i, n, u, P) that are needed in the RHSs of Eqs. (1.47) and (1.49) from the quantities that are actually updated during the integration process, i.e. from N, S_i and e . This is actually a not entirely trivial problem (sometimes called "recovery problem", "recovery" or "conservative-to-primitive transformation") that requires a numerical root finding algorithm. The exact algorithm depends on which equations are evolved and on the equation of state that is used. Our strategy in SPHINCS.BSSN is to express n and u in terms of the evolved variables N, S_i and e and the pressure P , substitute them into the (polytropic or piecewise polytropic) equation of state and use numerical rootfinding (we use Ridders' method [24]) to find the pressure value that solves this equation. Once this pressure value is found all physical quantities can be found by a simple backsubstitution. See Sec. 2.2.4 in [25] and Appendix A in [27] for a detailed description of the polytropic and the piecewise polytropic case, respectively.

1.2.1.4 Dissipative terms

So far, we have dealt exclusively with strictly non-dissipative hydrodynamics. Most astrophysical gas flows are overall very well described by such ideal fluids, but in reality shocks occur and, in a "microscopic" zoom into the shock front dissipative processes *do* occur which lead to an increase in entropy. Numerical methods need to mimic this behaviour, i.e. in smooth parts of the flow they should (ideally) be dissipationless, but they need to have a built-in mechanism which produces entropy in a shock front. This can be achieved by either some form of artificial viscosity or an (approximate or exact) Riemann solver. While both are valid possibilities [29, 55], we have decided to use a modern form of artificial viscosity that shares features with what is usually done in a finite volume scheme [56], in particular, our artificial viscosity treatment makes use of slope-limited reconstruction. This new approach to artificial viscosity has been extensively tested in our Newtonian SPH code MAGMA2 [57] which served as a technology testbed for SPHINCS_BSSN.

Artificial viscosity is actually one of the oldest techniques of computational physics [58], and while having had a questionable reputation for some time, it seems that it is becoming more popular again, though in more sophisticated forms than originally suggested [59, 60, 61, 62, 63, 64]. It is further worth pointing out that modern artificial viscosities share many similarities with approximate Riemann solvers [65].

Seemingly harmless sound waves can steepen into shocks during the hydrodynamic evolution, because the high-density parts try catch up with the slower low-density parts, see the sketch in the left panel of Fig. 1.1. Without any dissipation this process will keep going until the wave has steepened into a mathematical discontinuity where physical quantities change abruptly. In nature, dissipation becomes active on some small scale, so that the transition would be very sharp, usually much sharper than the lengths that can be numerically resolved, but not strictly discontinuous. The main idea of artificial viscosity is to add an "artificial pressure" q to the physical pressure P (wherever it occurs)

$$P \rightarrow P + q \tag{1.50}$$

in order to prevent the wave from becoming infinitely steep and instead keep it at a numerically treatable level. Or, in the words of John von Neumann and Robert Richtmyer [58]: "*Our idea is to introduce (artificial) dissipative terms into the equations so as to give shocks a thickness comparable to (but preferentially somewhat larger than) the spacing of the points of the network. Then the differential equations (more accurately, the corresponding difference equations) can be used for the entire calculation, just as if there were no shocks at all*".

We will not go into the explicit expressions for the artificial pressure q that we use, for this we refer to Sec. 2.1.1 in [27], we do, however, want to describe the basic ideas behind some of the recent artificial viscosity improvements. "Old style" SPH has been criticized for being overly dissipative. It is worth stating, however, that the SPH method as derived from the Lagrangian is completely inviscid, and in early SPH implementations the viscous terms were always switched on. For pedagogical

cal reasons, we will describe the improvements at the example of Newtonian SPH where the expressions are simplest, but all the ideas on how to improve artificial dissipation translate straight forwardly to the GR case [27]. In the Newtonian case, the viscous pressure typically has the form

$$q_a \propto \alpha_v \Delta v_{ab} \quad (1.51)$$

where α_v is a numerical parameter that needs to be of order unity at a shock (but not elsewhere) while Δv_{ab} quantifies the "velocity jump" between particle a and a neighbouring particle b (different expressions for the velocity jump are possible). The major concern is usually to not have dissipation where it is not needed. There are essentially three approaches to this. The first one is to multiply the quantity α_v with a "limiter" that is smart enough to decide, based on the local fluid properties, whether a particle is in a shock or not and, in the latter case, the limiter should have a very small or zero value to avoid dissipation. Different versions of such limiters have been suggested [66, 59, 35]. The second approach is to make α_v time-dependent [67], so that it decays exponentially, when it is not needed, to some small, possibly zero value, α_0 . This approach needs a "trigger" at each particle location that indicates whether more dissipation is needed. There are several possibilities for such triggers

- The original suggestion of Morris and Monaghan [67] was to use $-\nabla \cdot \vec{v}$ as a trigger so that dissipation switches on during compression. This, however, does not necessarily indicate a shock: gas can also be *adiabatically* compressed in which case no dissipation is wanted.
- Cullen and Dehnen [59] suggested (apart from some other improvements) to construct a trigger that is instead based on the time derivative $d(-\nabla \cdot \vec{v})/dt$. This quantity indicates a steepening flow convergence which is characteristic for a particle moving into a shock.
- Rosswog [34] suggested to use in addition to the *shock* trigger of Cullen and Dehnen [59], a *noise* trigger that switches on (to a smaller amount), if the flow becomes numerically noisy, even if there is no shock. Here, the main idea is to measure sign fluctuations of $\nabla \cdot \vec{v}$ in the neighborhood of a given particle: if there is a clean compression or expansion, all nearby particles have the same sign of $\nabla \cdot \vec{v}$, but a large number of positive and negative signs, instead, indicates noise.
- Rosswog [62] suggested to measure how the entropy of a particle evolves in time. Since we are modelling an ideal fluid, the entropy should be strictly conserved, this, however, is not numerically enforced by construction. That means that we can monitor the entropy conservation as a measure for the numerical quality of the flow and entropy non-conservation (either via shock or numerical noise) indicates that dissipation should be applied.

The third approach to avoid excessive dissipation [57], is actually very similar to the reconstruction procedure in Finite Volume schemes [56]. Instead of using the velocity difference between two particles for the velocity jump, $\Delta v_{ab} = \vec{v}_a - \vec{v}_b$, one uses instead the differences of the slope-limited velocities *reconstructed to the midpoint* between two particles, $\Delta \tilde{v}_{ab} = \tilde{\vec{v}}_a - \tilde{\vec{v}}_b$, as sketched in Fig. 1.1, right panel.

The slope-limited, first order reconstruction from the a -side reads

$$\tilde{v}_a^i = v_a^i + \Phi_{ab}(\partial_j v_a^i) \frac{1}{2}(r_b - r_a)^j \quad (1.52)$$

and correspondingly for the reconstruction from the b -side. For the slope limiter Φ_{ab} any of the standard slope limiters can be used in principle. The reconstruction can be extended to higher order, for example in the MAGMA2 code [57] we use a quadratic reconstruction.

In SPHINCS_BSSN we have implemented GR-versions of the second and the third of the above ideas. We also evolve our dissipation parameter triggered by a shock trigger similar to Cullen and Dehnen [59], enhanced by noise triggers as in Rosswog [34]. In addition, we perform linear reconstruction to the particle midpoint in which we use a minmod [68] slope limiter. Consult Sec. 2.1.1 in [27] for the explicit expressions of the artificial viscosity terms used in SPHINCS_BSSN.

1.2.2 Spacetime evolution

In general relativity, gravity is described as curvature of spacetime and the fundamental object is the spacetime metric, $g_{\mu\nu}$, from which the spacetime interval between infinitesimally close points can be calculated $ds^2 = g_{\mu\nu}dx^\mu dx^\nu$. From the metric tensor we can define the *Christoffel symbols*

$$\Gamma_{\mu\nu}^\lambda = \frac{g^{\lambda\sigma}}{2} \left[\frac{\partial g_{\mu\sigma}}{\partial x^\nu} + \frac{\partial g_{\nu\sigma}}{\partial x^\mu} - \frac{\partial g_{\mu\nu}}{\partial x^\sigma} \right], \quad (1.53)$$

from which we can calculate the *Riemann curvature tensor*

$$R^\lambda{}_{\sigma\mu\nu} = \frac{\partial \Gamma_{\sigma\nu}^\lambda}{\partial x^\mu} - \frac{\partial \Gamma_{\sigma\mu}^\lambda}{\partial x^\nu} + \Gamma_{\rho\mu}^\lambda \Gamma_{\sigma\nu}^\rho - \Gamma_{\rho\nu}^\lambda \Gamma_{\sigma\mu}^\rho. \quad (1.54)$$

Contracting the first and third index on the Riemann curvature tensor delivers the *Ricci tensor*, $R_{\mu\nu} = R^\lambda{}_{\mu\lambda\nu}$ and by contracting the two indices on the Ricci tensor one finds the *Ricci scalar* $R = g^{\mu\nu}R_{\mu\nu}$. These combine to define the *Einstein tensor* that is related to the stress-energy tensor in the full covariant 4-dimensional set of Einstein field equations

$$G_{\mu\nu} = R_{\mu\nu} - \frac{1}{2}g_{\mu\nu}R = 8\pi T_{\mu\nu}, \quad (1.55)$$

which, in turn, is the starting point for any spacetime evolution code.

These equations are 4-dimensional and it is, therefore, not possible to evolve them like a normal initial value problem, where one provides 3-dimensional data at a given time and evolves it forward to the next time. What we can do to achieve this

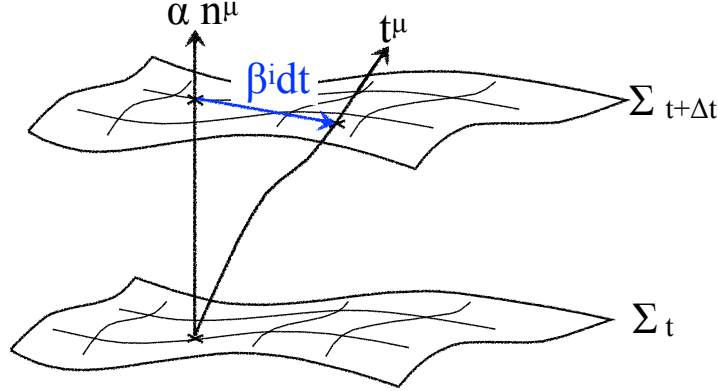


Fig. 1.2: 3+1 foliation of the spacetime. The spacetime is sliced into spacelike hypersurfaces which are integrated forward in time. The lapse function α measures the proper time along the normal n^μ , the shift vector β^i measures the displacement, on consecutive hypersurfaces, between the observer time lines t^μ and the normal lines n^μ .

is to split the spacetime into 3+1 dimensions⁷, that is we write the line element as

$$ds^2 = g_{\mu\nu} dx^\mu dx^\nu = (-\alpha^2 + \beta_i \beta^i) dt^2 + 2\beta_i dt dx^i + \gamma_{ij} dx^i dx^j, \quad (1.56)$$

where we have introduced the lapse function, α , the shift vector, β^i , and the spatial 3-metric, γ_{ij} . This foliates spacetime into non-intersecting spacelike hypersurfaces Σ labeled by the coordinate time, t , see the sketch in Fig. 1.2. Each spatial slice has a future pointing normal vector, n^μ , whose coordinates are $n^\mu = (1/\alpha, -\beta^i/\alpha)$. In this picture the lapse α measures the elapsed proper time between two nearby spatial slices (in the normal direction), the shift vector, β^i , is the relative velocity of Eulerian observers and the lines of constant spatial coordinates and the spatial metric, γ_{ij} , measure proper distance within the slices.

The curvature that is intrinsic to the slices is, of course, given by the 3-dimensional Riemann tensor defined in terms of the 3-metric γ_{ij} . However, there is also an extrinsic curvature associated with how the 3-dimensional slices are embedded in the overall 4-dimensional spacetime. Remarkably, this can be described in terms of another 3-dimensional tensor, K_{ij} , that can be defined as the projection of the gradient of the normal vector onto the spatial slice

$$K_{\mu\nu} := -P_\mu^\lambda n_{\nu;\lambda}, \quad (1.57)$$

⁷ This is certainly not the only possible way to convert the Einstein equations into an initial value problem, but it is a very common approach and the one we have chosen here.

where P_μ^λ is the projection operator,

$$P_\mu^\lambda := \delta_\mu^\lambda + n^\lambda n_\mu. \quad (1.58)$$

Note that even though the extrinsic curvature is defined as a 4-dimensional object in Eq. (1.57), it is indeed a 3-dimensional object with $K^{00} = K^{0i} = 0$ and can be referred to as K^{ij} . K_{00} and K_{0i} on the other hand are not zero, but the components of K_{ij} can still be obtained by using only the spatial metric, γ_{ij} , to lower the indices of K^{ij} .

Leaving out the details (see the excellent text books [17, 18] for more information) it is then possible to split the 10 original second order Einstein equations into 12 first order hyperbolic evolution equations

$$\partial_t \gamma_{ij} = -2\alpha K_{ij} + D_i \beta_j + D_j \beta_i, \quad (1.59)$$

$$\begin{aligned} \partial_t K_{ij} = & -D_i D_j \alpha + \alpha \left[{}^{(3)}R_{ij} + K K_{ij} - 2K_{ik} K_j^k \right] \\ & + 4\pi\alpha [\gamma_{ij}(S - \rho) - 2S_{ij}] + \beta^k \partial_k K_{ij} + K_{ki} \partial_j \beta^k + K_{kj} \partial_i \beta^k, \end{aligned} \quad (1.60)$$

where D is the 3-dimensional covariant derivative related to γ_{ij} , $\rho = n^\mu n^\nu T_{\mu\nu}$, $S_{\mu\nu} = P_\mu^\lambda P_\nu^\sigma T_{\lambda\sigma}$ and $S = S_\mu^\mu$ and 4 elliptical constraint equations

$${}^{(3)}R + K^2 - K_{ij} K^{ij} = 16\pi\rho \quad (1.61)$$

$$D_j (K^{ij} - \gamma^{ij} K) = 8\pi j^i, \quad (1.62)$$

where $j^\mu = -P^{\mu\lambda} n^\nu T_{\lambda\nu}$. Equations (1.59) and (1.60), as written here, are due to York [69] and are known as the ADM equations after Arnowitt, Deser and Misner. Given initial data for γ_{ij} and K_{ij} on a 3-dimensional spatial slice, the ADM equations can in principle be used to evolve the spacetime forward in time. Equation (1.61) is the *Hamiltonian or energy constraint* and equation (1.62) is the so-called *momentum constraint*. These do not involve any time derivatives but rather provide a set of equations that any physical data has to satisfy at any point in time. This is similar, for example, to the case of magneto-hydrodynamics, where one has evolution equations that have to fulfill the $\nabla \cdot \vec{B} = 0$ -constraint at any point in time.

Note that the York form of the ADM equations, also known as standard ADM, differ from the original ADM equations [70] by a term proportional to the Hamiltonian constraint. Hence they are physically equivalent but not mathematically or numerically equivalent. This is because the Hamiltonian constraints contains second derivatives that changes the principal part and therefore the mathematical properties of the equations.

There is a lot of freedom in choosing which of the 12 components of γ_{ij} and K_{ij} to provide initial data for and which of the components to solve for using the constraint equations. Luckily, once constraint satisfying initial data are set up, evolution of that data using the ADM evolution equations will guarantee, in the absence of numerical errors, that the evolved data remains constraint satisfying. Of course numerical errors are unavoidable, which means that any numerical evolution will always have

some constraint violations. In that case the constraint violations can be used to monitor the numerical quality of the simulation.

The only problem with the ADM equations is that they do not actually work in practice. They can be shown (see for example [17]) to be only *weakly hyperbolic* and hence they are not a well posed formulation of the Einstein equation. An alternative formulation due to Baumgarte, Shapiro, Shibata and Nakamura, the so-called BSSN formulation [18, 20], has proven to be a robust choice for many codes and has therefore become rather popular. In the BSSN formulation a conformal rescaling is introduced

$$\tilde{\gamma}_{ij} = e^{-4\phi} \gamma_{ij}, \quad (1.63)$$

where ϕ is defined in terms of the determinant of the physical three-metric, γ , as $\phi = \frac{1}{12} \log \gamma$. With this choice the determinant of the conformal metric becomes $\tilde{\gamma} = 1$. In addition, the extrinsic curvature is separated into its trace and its tracefree part and conformally rescaled

$$\tilde{A}_{ij} = e^{-4\phi} A_{ij} = e^{-4\phi} \left(K_{ij} - \frac{1}{3} \gamma_{ij} K \right). \quad (1.64)$$

The final addition is to also evolve the three quantities

$$\tilde{\Gamma}^i = \tilde{\gamma}^{jk} \tilde{\Gamma}_{jk}^i = -\partial_j \tilde{\gamma}^{jj}, \quad (1.65)$$

where $\tilde{\Gamma}_{jk}^i$ is the Christoffel symbols related to the conformal metric. That is, the BSSN evolution variables are ϕ , $\tilde{\gamma}$, K , \tilde{A} and $\tilde{\Gamma}^i$, and result in the following set of evolution equations

$$\partial_t \phi = -\frac{1}{6} (\alpha K - \partial_i \beta^i) + \beta^i \bar{\partial}_i \phi, \quad (1.66)$$

$$\partial_t \tilde{\gamma}_{ij} = -2\alpha \tilde{A}_{ij} + \tilde{\gamma}_{ik} \partial_j \beta^k + \tilde{\gamma}_{jk} \partial_i \beta^k - \frac{2}{3} \tilde{\gamma}_{ij} \partial_k \beta^k + \beta^k \bar{\partial}_k \tilde{\gamma}_{ij}, \quad (1.67)$$

$$\begin{aligned} \partial_t K = & -e^{-4\phi} \left(\tilde{\gamma}^{ij} [\partial_i \partial_j \alpha + 2\partial_i \phi \partial_j \alpha] - \tilde{\Gamma}_{(n)}^i \partial_i \alpha \right) \\ & + \alpha \left(\tilde{A}_j^i \tilde{A}_i^j + \frac{1}{3} K^2 \right) + \beta^i \bar{\partial}_i K + 4\pi \alpha (\rho + s), \end{aligned} \quad (1.68)$$

$$\begin{aligned} \partial_t \tilde{A}_{ij} = & e^{-4\phi} \left[-\partial_i \partial_j \alpha + \tilde{\Gamma}_{ij}^k \partial_k \alpha + 2(\partial_i \alpha \partial_j \phi + \partial_j \alpha \partial_i \phi) + \alpha R_{ij} \right]^{\text{TF}} \\ & + \alpha (K \tilde{A}_{ij} - 2\tilde{A}_{ik} \tilde{A}_j^k) + \tilde{A}_{ik} \partial_j \beta^k + \tilde{A}_{jk} \partial_i \beta^k - \frac{2}{3} \tilde{A}_{ij} \partial_k \beta^k \\ & + \beta^k \bar{\partial}_k \tilde{A}_{ij} - e^{-4\phi} \alpha 8\pi \left(T_{ij} - \frac{1}{3} \gamma_{ij} s \right), \end{aligned} \quad (1.69)$$

$$\begin{aligned} \partial_t \tilde{\Gamma}^i = & -2\tilde{A}^{ij} \partial_j \alpha + 2\alpha \left(\tilde{\Gamma}_{jk}^i \tilde{A}^{jk} - \frac{2}{3} \tilde{\gamma}^{ij} \partial_j K + 6\tilde{A}^{ij} \partial_j \phi \right) \\ & + \tilde{\gamma}^{jk} \partial_j \partial_k \beta^i + \frac{1}{3} \tilde{\gamma}^{ij} \partial_j \partial_k \beta^k - \tilde{\Gamma}_{(n)}^j \partial_j \beta^i + \frac{2}{3} \tilde{\Gamma}_{(n)}^i \partial_j \beta^j \\ & + \beta^j \bar{\partial}_j \tilde{\Gamma}^i - 16\pi \alpha \tilde{\gamma}^{ij} s_j, \end{aligned} \quad (1.70)$$

where

$$\rho = \frac{1}{\alpha^2} (T_{00} - 2\beta^i T_{0i} + \beta^i \beta^j T_{ij}), \quad (1.71)$$

$$s = \gamma^{ij} T_{ij}, \quad (1.72)$$

$$s_i = -\frac{1}{\alpha} (T_{0i} - \beta^j T_{ij}), \quad (1.73)$$

and $\beta^i \bar{\partial}_i$ denote partial derivatives that are "upwinded" based on the shift vector. This means that the stencil used for finite differencing is shifted by one in the direction of the shift. As an example of this, look at second order finite differencing, where a derivative in the x-direction at grid point x_i would normally be approximated by the centered finite difference

$$\left. \frac{\partial f}{\partial x} \right|_{x=x_i} \approx \frac{-f_{i-1} + f_{i+1}}{2\Delta x} + O(\Delta x^2). \quad (1.74)$$

If the shift is positive we instead use the "upwinded" finite difference approximation

$$\left. \bar{\partial} f \right|_{x=x_i} \approx \frac{-3f_i + 4f_{i+1} - f_{i+2}}{2\Delta x} + O(\Delta x^2), \quad (1.75)$$

whereas if the shift is negative we use

$$\left. \frac{\partial f}{\partial x} \right|_{x=x_i} \approx \frac{f_{i-2} - 4f_{i-1} + 3f_i}{2\Delta x} + O(\Delta x^2). \quad (1.76)$$

The superscript ‘‘TF’’ in the evolution equation of \tilde{A}_{ij} denotes the trace-free part of the bracketed term. Note that there is a slight subtlety to the treatment of $\tilde{\Gamma}^i$. We introduce

$$\tilde{\Gamma}_{(n)}^i = \tilde{\gamma}^{jk} \tilde{\Gamma}_{jk}^i, \quad (1.77)$$

i.e. a numerical recalculation of the contracted conformal Christoffel symbols from the current conformal metric. This is used instead of $\tilde{\Gamma}^i$ whenever derivatives of $\tilde{\Gamma}^i$ are not needed. In all other places, i.e. when finite differences are needed, the evolved variables, $\tilde{\Gamma}^i$, are used directly. This helps with numerical stability and makes the constraint $\tilde{\Gamma}^i = -\partial_j \tilde{\gamma}^{ij}$ better behaved. Finally $R_{ij} = \tilde{R}_{ij} + R_{ij}^\phi$, where

$$\tilde{\Gamma}_{ijk} = \frac{1}{2} (\partial_k \tilde{\gamma}_{ij} + \partial_j \tilde{\gamma}_{ik} - \partial_i \tilde{\gamma}_{jk}), \quad (1.78)$$

$$\tilde{\Gamma}_{ij}{}^k = \tilde{\gamma}^{kl} \tilde{\Gamma}_{ijl}, \quad (1.79)$$

$$\tilde{\Gamma}_{jk}^i = \tilde{\gamma}^{il} \tilde{\Gamma}_{ljk}, \quad (1.80)$$

$$\tilde{\Gamma}_{(n)}^i = \tilde{\gamma}^{jk} \tilde{\Gamma}_{jk}^i, \quad (1.81)$$

$$\begin{aligned} \tilde{R}_{ij} = & -\frac{1}{2} \tilde{\gamma}^{kl} \partial_k \partial_l \tilde{\gamma}_{ij} + \tilde{\gamma}_{k(i} \partial_j) \tilde{\Gamma}^k + \tilde{\Gamma}_{(n)}^k \tilde{\Gamma}_{(ij)k} + \tilde{\Gamma}_{il}^k \tilde{\Gamma}_{jk}{}^l \\ & + \tilde{\Gamma}_{jl}^k \tilde{\Gamma}_{ik}{}^l + \tilde{\Gamma}_{il}^k \tilde{\Gamma}_{kj}{}^l, \end{aligned} \quad (1.82)$$

$$\begin{aligned} R_{ij}^\phi = & -2 \left(\partial_i \partial_j \phi - \tilde{\Gamma}_{ij}^k \partial_k \phi \right) - 2 \tilde{\gamma}_{ij} \tilde{\gamma}^{kl} (\partial_k \partial_l \phi - \tilde{\Gamma}_{kl}^m \partial_m \phi) \\ & + 4 \partial_i \phi \partial_j \phi - 4 \tilde{\gamma}_{ij} \tilde{\gamma}^{kl} \partial_k \phi \partial_l \phi, \end{aligned} \quad (1.83)$$

where the standard notation for symmetrization, $A_{(ij)} = (A_{ij} + A_{ji})/2$, has been used. The additional constraints associated with the conformal metric, $1 - \tilde{\gamma} = 0$, and conformal traceless part of the extrinsic curvature, $\tilde{A} = \tilde{\gamma}^{ij} \tilde{A}_{ij} = 0$, are enforced at every substep of the time integrator.

Note that a slight variation of BSSN, where $W = \gamma^{-1/6}$ is used as an evolution variable instead of ϕ is implemented in the `SPHINCS_BSSN` code as well. This variant seems to be better behaved near the puncture of a black hole, but is not expected to have a significant effect for binary neutron star mergers.

The BSSN evolution equations above do not give a prescription for how to choose the gauge variables, α and β^i . In order to complete the system, we add the simplest form of the so-called *moving puncture gauges*, i.e.

$$\partial_t \alpha = -2\alpha K \quad (1.84)$$

and

$$\partial_t \beta^i = \frac{3}{4} (\tilde{\Gamma}^i - \eta \beta^i). \quad (1.85)$$

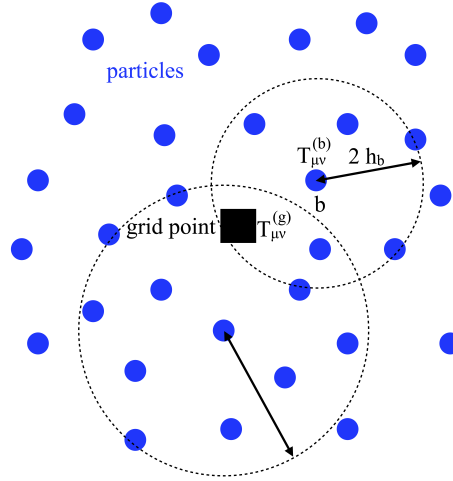


Fig. 1.3: Particle-to-mesh step: the energy momentum tensor $T_{\mu\nu}$ is naturally known at the particle positions (blue circles), since it is needed as a source of the spacetime evolution equations, the particle values need to be "transferred" to the grid points (black square). This is achieved by an LRE-MOOD approach, see the main text for an explanation.

1.2.3 Particle-mesh interaction

Since we are solving the hydrodynamic equations by means of Lagrangian particles, but evolve the spacetime on a mesh, the particles and the mesh need to continuously exchange information. As one sees from Eqs. (1.47) and (1.49), the particle evolution equations need the metric and its derivatives, which are known at grid points, while the spacetime/BSSN-evolution equations, see Eqs (1.68), (1.69) and (1.70), need the matter's energy momentum tensor, Eq. (1.30), which is known at the particle positions. In other words, the metric and its derivatives need to be interpolated –at every Runge-Kutta substep– to the particle positions ("mesh-to-particle"-, or M2P-step) and the energy momentum tensor needs to be mapped to grid points based on the values at the surrounding particles ("particle-to-mesh"-, or P2M-step). The simpler of the two is the M2P-step. In `SPHINCS_BSSN` it is performed via a 5th order Hermite interpolation, that we have developed in [25] extending the work of [71]. Contrary to a standard Lagrange polynomial interpolation, the Hermite interpolation guarantees that the metric remains twice differentiable as particles pass from one grid cell to another and therefore this sophisticated interpolation avoids the introduction of additional noise. The details of our approach are explained in Section 2.4 of [25] to which we refer the interested reader.

The P2M-step is more complicated since the particle distribution is continuously changing and the particles are in particular not arranged on a regular lattice. Our

original approach [25, 26, 27] was to use sophisticated kernels that we borrowed from vortex methods [72], but we have recently [28] further refined our P2M-step. Our new approach is based on a "local regression estimate" (LRE), where for a given polynomial order, we determine the $T_{\mu\nu}$ value on the grid points by the requirement that it is the best fit (according to a suitable error measure) to the surrounding particle values, see Fig. 1.3. The remaining question is then: which polynomial order should be used? Also here we follow an optimization approach: we perform trial LRE-mappings for all orders up to a maximal order (= 4), and out of those trial mappings we select the one that agrees best with the surrounding particles. This selection process for the polynomial order is called "Multidimensional Optimal Order Detection" (MOOD), and we therefore call our P2M-approach "LRE-MOOD".

1.2.3.1 LRE-mapping

The basic idea is to assume that the particle values are given by some unknown function f , which can be expanded in a Taylor series around a grid point located at \vec{r}_G

$$f(\vec{r}) = f^G + (\partial_i f)^G (\vec{r} - \vec{r}^G)^i + \frac{1}{2} (\partial_{ij} f)^G (\vec{r} - \vec{r}^G)^i (\vec{r} - \vec{r}^G)^j + \text{h.o.t.} \quad (1.86)$$

The terms like $(\vec{r} - \vec{r}^G)^i$ can be interpreted as a polynomial basis P_l , shifted to the grid point \vec{r}_G , with coefficients α_l that contain the derivatives of f . The approximation, "optimized at the grid point G", can then be written as

$$\tilde{f}^G(\vec{r}) = \sum_{l=0}^{l_{\max}} \alpha_l^G P_l^G(\vec{r}). \quad (1.87)$$

Here l_{\max} is the number of degrees of freedom and for d spatial dimensions and a maximum polynomial order m , it is given by

$$l_{\max} = \frac{(d+m)!}{d!m!}. \quad (1.88)$$

That is we have 1, 4, 10, 20 and 35 degrees of freedom for constant, linear, quadratic, cubic and quartic polynomials. We want the α_l to be an optimal fit to the surrounding particles, therefore we minimize at each grid point the error measure

$$\varepsilon^G \equiv \sum_p [f_p - \tilde{f}^G(\vec{r}_p)]^2 W_{pG}, \quad (1.89)$$

where the f_p are the function values at the particle positions and W_{pG} is a smooth, positive definite function (e.g. a typical SPH kernel) that gives particles that are closer to the grid point a larger weight than to further away particles. The optimal coefficients, α^G , are then found from the condition

$$\left(\frac{\partial \mathcal{E}^G}{\partial \alpha_i} \right)_G \stackrel{!}{=} 0, \quad (1.90)$$

which yields [28]

$$\alpha_i^G = (M_{ik})^{-1} B_k, \quad (1.91)$$

where the "moment matrix" reads

$$M_{ik} = \sum_p P_i^G(\vec{r}_p) P_k^G(\vec{r}_p) W_{pG} \quad (1.92)$$

and the vector that contains the information about the function values reads

$$B_k = \sum_p f_p P_k^G(\vec{r}_p) W_{pG}. \quad (1.93)$$

The moment matrix can be close to singular, therefore we solve for the α_i by means of a singular value decomposition [24]. For more details and some examples of function approximations, we refer to the appendix of our recent paper [28].

1.2.3.2 Multi-dimensional optimal order detection (MOOD)

While we have just addressed how to determine the best coefficients for a given polynomial order, we still need to discuss how we decide which polynomial order is chosen. Here we follow an approach that is sometimes used in computational hydrodynamics [73], where the basic idea is to try a number of possibilities, dismiss not-admissible solutions (e.g. unphysical ones with $\rho < 0$) and pick the most accurate out of the admissible solutions. To take this decision, we use the following error measure:

$$\begin{aligned} E^{G,m} &\equiv \sum_p W_{pG} \left[\sum_{\mu,\nu} \left\{ \tilde{T}_{\mu\nu}^{G,m}(\vec{r}_p) - T_{\mu\nu,p} \right\}^2 \right] \\ &= \sum_p W_{pG} \left[\sum_{\mu,\nu} \left\{ \left(\tilde{\beta}_{\mu,\nu}^{G,m} \cdot P^G(\vec{r}_p) \right) - T_{\mu\nu,p} \right\}^2 \right], \end{aligned} \quad (1.94)$$

where W_{pG} is, as before, a smooth positive definite function. In other words, for each polynomial order m , we use the optimal coefficients at the grid point to estimate the function values *at each particle position* for those particles that contribute to the grid point and from the difference between these estimates and the real function values at the particle positions we calculate an error measure. The aim is then to select the polynomial order with the smallest error measure that is physically admissible. There is, however, one more subtlety....

Identifying the stellar surface

We have tested the just described approach extensively and we noted when sim-

ulating neutron stars that in very few cases, when particles at the stellar surface contribute to grid cells lying just beneath the surface, the lowest error result can be an outlier value compared to the surrounding grid points. Therefore, we treat surface grid points differently: here we only apply the lowest polynomial order. This, however, requires the identification of which grids points are close to the stellar surface. We do this by checking which grid cells have many contributions from "surface particles", so we need to answer the question: *How can we identify particles at the stellar surface?*

The decisive insight to identify the surface is that at this place "particles are missing on one side" and that this will deteriorate standard SPH-approximations such as Eq. (1.13). If a particle is well engulfed in all directions by other particles, we will find a very good numerical approximation to an analytical result and –vice versa– a bad approximation indicates that the particle is located near a surface. In practice, we calculate a numerical approximation to $\nabla \cdot \vec{r} = 3$ and we use the gradient estimate Eq. (1.13) for the numerical approximation

$$(\nabla \cdot \vec{r})_a = \sum_b \frac{V_b}{N_b} (\vec{r}_b - \vec{r}_a) \cdot \nabla_a W_{ab}(h_a). \quad (1.95)$$

From the relative error

$$\delta_a \equiv \frac{|(\nabla \cdot \vec{r})_a - 3|}{3} \quad (1.96)$$

we calculate the average deviation $\langle \delta \rangle_G = (\sum_{b=1}^n \delta_b) / n$, where n is the number of particles that contribute to the error measure Equation (1.94). We use $\langle \delta_G \rangle > 0.05$ as an accurate and robust identification of a grid point near the fluid surface. For such grid points we only use polynomial order $m = 0$.

1.3 Tests and first applications

We show here some of the test cases to verify the correct implementation of the above described methods, more tests can be found in [25, 27]. We further show some of the first applications to neutron star mergers.

1.3.1 3D shock tube

With exactly known solutions, shock tubes are excellent tests to verify a correct implementation of the hydrodynamic equations. We perform here a 3D relativistic version of "Sod's shocktube" [74] which has become a widespread benchmark for relativistic hydrodynamics codes [75, 76, 37, 77, 78]. The test uses a polytropic exponent $\Gamma = 5/3$ and as initial conditions

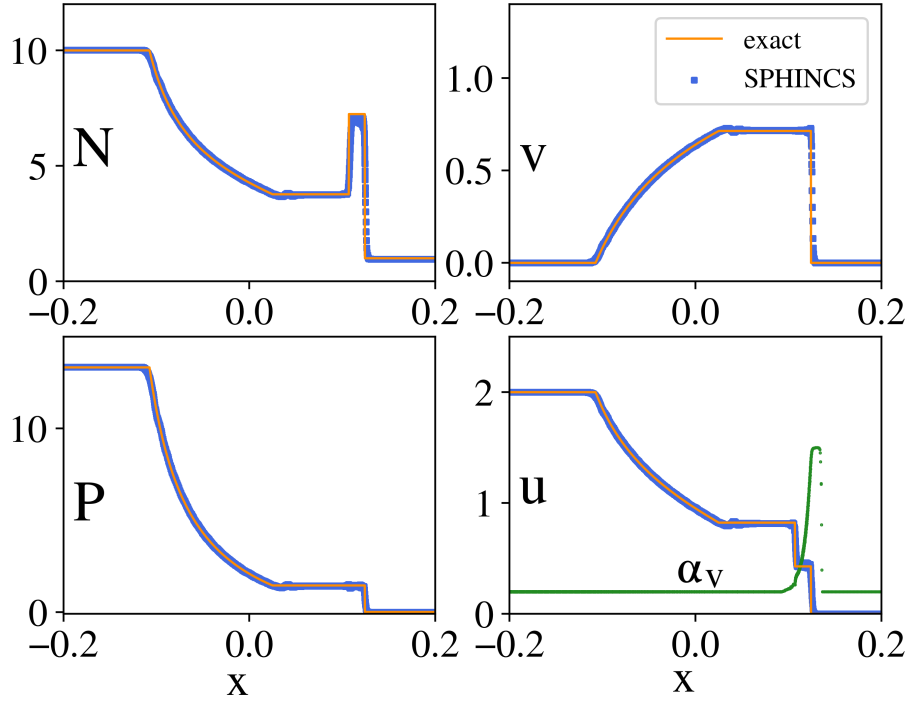


Fig. 1.4: 3D, relativistic shocktube test. The exact solution is shown as orange lines, while the numerical results for the computing frame baryon number density N , the velocity v , the pressure P and the specific internal energy u are shown as blue squares. All particles are shown. We also show in last panel the dissipation parameter α (in green): it "switches on" just directly ahead of the shock, and then very quickly decays to the floor level value.

$$[N, P] = \begin{cases} \left[10, \frac{40}{3}\right], & \text{for } x < 0 \\ \left[1, 10^{-6}\right] & \text{for } x \geq 0, \end{cases} \quad (1.97)$$

with velocities initially being zero everywhere. We place particles with equal baryon numbers on close-packed lattices as described in [34], so that on the left side the particle spacing is $\Delta x_L = 0.0005$ and we have 12 particles in both y - and z -direction⁸. This test is performed with the full 3+1 dimensional code, but using a fixed Minkowski metric. The result at $t = 0.15$ is shown in Fig. 1.4 with the SPHINCS_BSSN results marked with blue squares and the exact solution [78] with the orange line. In the last panel we also show the dissipation parameter α_v (in green): it switches on sharply just *ahead* of the shock front and then, once the shock

⁸ The particle spacing on the right side is then given by the density jump and the requirement that particles have equal baryon numbers.

wave has passed, very rapidly decays to the chosen floor value. Overall there is very good agreement with practically no spurious oscillations. There is only a small amount of "noise" directly after the shock front. This is to some extent unavoidable, since here the particles have to re-arrange themselves from their pre-shock close-packed configuration into their preferred post-shock configuration which goes along with some mild sideways motion.

1.3.2 Oscillating neutron stars

In order to test the full code, i.e. the relativistic hydrodynamics, the spacetime evolution and their mutual coupling via the mappings from the grid to the particles and from the particles to the grid, we have performed simulations of single oscillating neutron stars. For this problem oscillation frequencies are known from independent, linear perturbation approaches [79?] which serve as a measure of the accuracy of our approach. We solve the Tolman-Oppenheimer-Volkoff (TOV) equations [80, 81] for a star in equilibrium which is then used to set up initial data for the particles and the spacetime grid. Due to truncation error the star does not remain in exact equilibrium and different eigenmodes of the star are excited at eigenfrequencies that depend on the equation of state and the mass of the star. With the choice of $K = 100$ and a central density of $\rho_c = 1.28 \times 10^{-3} = 7.91 \times 10^{14} \text{g/cm}^3$ we get a star with a gravitational mass of $1.4 M_\odot$ and a baryonic mass of $1.506 M_\odot$.

We performed 3 simulations with varying resolution of both the number of particles and the grid. For the particles we used 500k (low), 1M (medium) and 2M (high) particles. In all cases we used a grid with outer boundaries (in all directions) at 160 in code units, corresponding to 236 km. We used 4 levels of refinement with the star being completely contained within the finest grid. The resolution on the finest grid was $0.4 \approx 590$ m (low), $0.317 \approx 468$ m (medium) and $0.25 \approx 369$ m (high). The smallest smoothing length in each case was about 310 m (low), 255 m (medium) and 208 m (high). We evolved the stars up to physical times of almost 30 ms.

The results are shown in Fig. 1.5. In the top plot we show the relative difference between the maximal density, ρ_{\max} , and the initial maximal density, ρ_0 , as a function of time for the three runs. Here light blue is low, orange is medium and dark blue is high resolution. As expected, the amplitudes of the oscillations decrease with higher resolution (≈ 0.002 for 2M particles) and multiple modes at different frequencies are excited. Taking a Fourier transform of $(\rho_{\max} - \rho_0)/\rho_0$ results in the spectrum shown in the bottom plot of Fig. 1.5. We see one weak peak as well as five strong peaks, all at frequencies that agree very well with the frequencies of the fundamental mode and the five first harmonics calculated⁹ with the linear perturbation code written by Panagiota Kolitsidou [?]. The reference values for the known frequencies are indicated with black vertical lines in the plot. Quantitative error measures for the known frequencies are provided in Table 1.1. Note that even at the lowest

⁹ Kindly provided to us by Kostas Kokkotas and Nick Stergioulas.

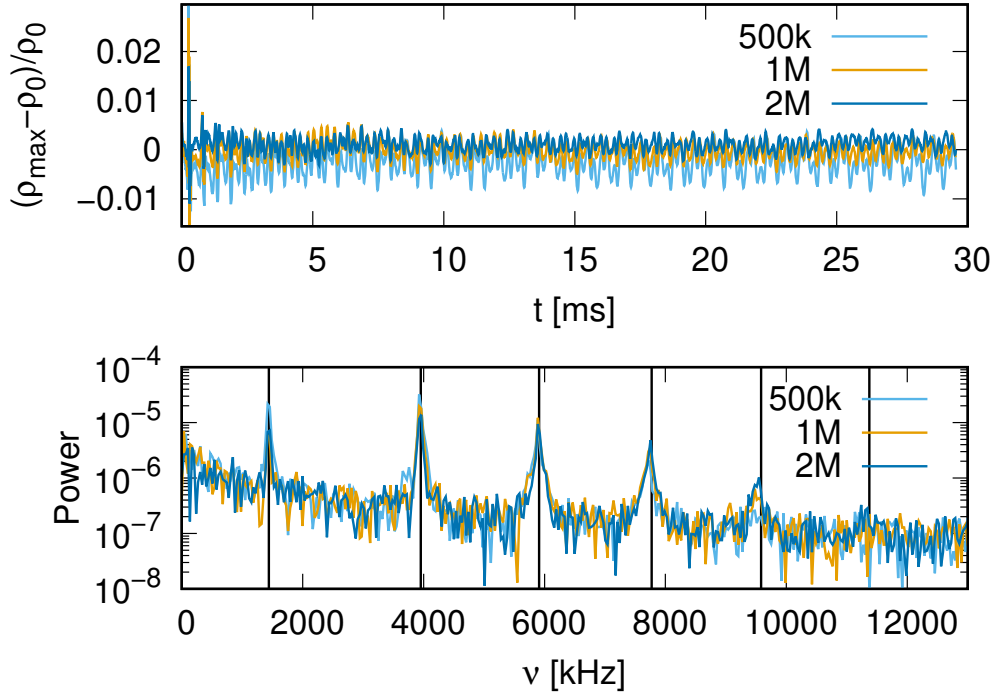


Fig. 1.5: Top plot: The relative difference between the maximal density ρ_{\max} and the initial maximal density, ρ_0 , for the TOV star as function of time in units of ms. Bottom plot: The power in the Fourier spectrum as function of frequency in units of Hz. In both plots the light blue line is for 500k, the orange is for 1M and the dark blue is for 2M particles. In the bottom plot, the vertical lines indicate (from left to right) the position of the expected frequency for the fundamental mode at 1.442 kHz, the first harmonic at 3.952 kHz, the second harmonic at 5.913 kHz, the third harmonic at 7.771 kHz, the fourth harmonic at 9.584 kHz and the fifth harmonic at 11.373 kHz. Even though the fifth harmonic is barely visible, we can still extract the frequency to better than 1% accuracy (see Table 1.1) from the simulation data.

resolution, the frequencies agree to better than 1% with the reference solution and they further improve with resolution.

In Fig. 1.6 we show a projection to the xy -plane of the particle distribution at the end of the simulation (left plot) and a comparison between the initial (black) and final (red) density as a function of radius (right plot). The final time, $t = 29.55$ ms, corresponds to more than 42 oscillation periods at the fundamental mode frequency. Note that, despite the long evolution time, the surface of the TOV star is extremely well behaved with no "outlier" particles (the plot shows all the particles). In contrast, the neutron star surface in *Eulerian* simulations is a perpetual source of numerical

Table 1.1: Oscillation frequencies: fundamental mode (F), first, second, third, fourth and fifth harmonic (H1, H2, H3, H4 and H5) frequencies (from [?]) are given in Hz in the "Reference" column. For each resolution we list the extracted frequency of all modes (number before \pm), as well as an estimate of the accuracy of its extraction (number after \pm). Finally the relative error between the extracted frequency and the reference frequency is given in the parenthesis. Note that even at the lowest resolution the agreement of SPHINCS_BSSN results with the reference solution is better than 1%.

Mode	Reference (Hz)	500k (Hz)	1M (Hz)	2M (Hz)
F	1441.9	1435.9 ± 2.5 (0.4)	1441.5 ± 6.1 (0.03)	1439.0 ± 4.0 (0.2)
H1	3952.4	3937.0 ± 3.3 (0.4)	3942.1 ± 5.5 (0.3)	3945.4 ± 4.2 (0.2)
H2	5912.5	5890.1 ± 2.7 (0.4)	5895.7 ± 5.9 (0.3)	5901.8 ± 4.4 (0.2)
H3	7770.6	7713.4 ± 5.0 (0.7)	7733.7 ± 6.1 (0.5)	7750.4 ± 4.0 (0.3)
H4	9583.9	9571.5 ± 32 (0.1)	9532.4 ± 52 (0.5)	9537.8 ± 21 (0.5)
H5	11373.1	11345.9 ± 19 (0.2)	11357.5 ± 31 (0.1)	11326.3 ± 36 (0.4)

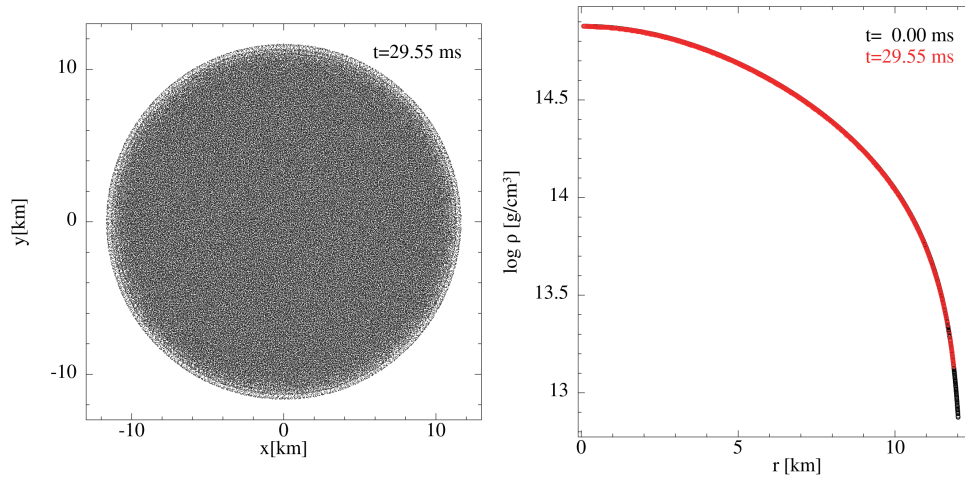


Fig. 1.6: The left plot shows a projection of the particle distribution of a 2M particle simulation (all particles are shown) at the final time, $t = 29.55$ ms. This time corresponds to more than 42 oscillation periods of the fundamental mode. Note that the neutron star surface has remained perfectly well behaved and the density distribution at late time (red) is nearly identical to the initial condition (black).

trouble where often (completely spurious) ”winds” are driven away from the star. From the right plot it is clear that the density distribution has changed very little over the duration of the simulation. The main difference is that particles near the surface have moved inward by a very small amount compared to the starting position, but overall the density distribution has remained very well-behaved and is essentially identical to the initial condition.

1.3.3 Neutron star mergers

One of the key motivations behind the `SPHINCS_BSSN` development efforts are the multi-messenger signatures of merging neutron star binaries. We will show here two examples, one merger where the remnant remains stable until the end of the simulation and another one where the encounter results in a prompt collapse to a black hole.

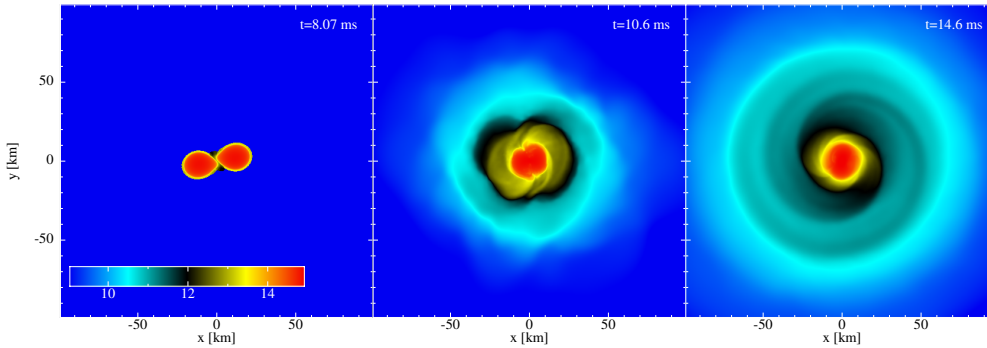


Fig. 1.7: Merger of an irrotational binary system with $2 \times 1.3 M_{\odot}$ with the APR3 equation of state. Shown is the density distribution in the orbital plane.

1.3.3.1 Merger with stable remnant

As an example of a neutron star merger that results in a surviving remnant, we show a binary of $2 \times 1.3 M_{\odot}$ with the piecewise polytropic representation [82] of the APR3 equation of state [83], where we add a thermal pressure/internal energy component with a thermal polytropic exponent $\Gamma_{\text{th}} = 1.75$, see Fig. 1.7. The spacetime/matter initial conditions for this binary system were calculated using the FUKA code [84], subsequently the particles were placed according to the ”artificial pressure method” [57, 28] with the code `SPHINCS_ID`. We start from an initial separation $a_0 = 45$ km and use 2 million SPH particles to model the matter evolution while for the space-

time evolution we initially employ seven levels of mesh refinement with 193 points in each direction. During the merger and the subsequent evolution, the spacetime becomes more extreme and `SPHINCS_BSSN` automatically increases the number of refinement levels to eight, see Sec. 2.5 in [28] for more information on our mesh refinement algorithm.

Fig. 1.7 shows the density evolution (in the orbital plane) and in the top of Fig. 1.8 we show how the maximum density and the minimum value of the lapse function evolve. As the stars approach each other, the lapse continuously decreases, while the peak density stays essentially constant. The merger results in a strong initial compression (by $\sim 25\%$ in the density), a subsequent "bounce back" during which the peak density drops below the initial single-star density, and then a continuous increase which levels off to a constant value at ~ 15 ms after the merger. The evolution of the lapse function during the merger is anti-correlated with the peak density: during maximum compression the lapse drops to a minimum value of 0.42 and reaches after ~ 15 ms an asymptotic value of 0.45.

In the bottom plot of Fig. 1.8 we show, in light blue, the plus- and, in orange, the cross-polarization of the strain times the distance to the source, r . The gravitational waves have been extracted from the simulation via the Newman–Penrose Weyl scalar Ψ_4 at an extraction sphere of $R_{\text{extr}} = 150 \approx 221.5$ km, see the appendix A of [26] for more details and we have used `kuibit` [85] for their analysis. At the earliest stages ($t < -7$ ms; $t = 0$ marking the peak GW emission) there is a small spurious transient introduced by the initial conditions, subsequently one recognizes the expected "chirp" signal with a long ring-down phase.

1.3.3.2 Merger with prompt black hole formation

As an example of a system that undergoes prompt collapse to a black hole, we show the merger of a $2 \times 1.5 M_{\odot}$ binary with the same equation of state, initial separation, particle number and initial grid setup as in Sec. 1.3.3.1. As this system is massive enough to undergo prompt collapse to a black hole, more refinement levels are added automatically as the collapse proceeds until, at the end, we have 11 levels of refinement. Again see Sec. 2.5 in [28] for the details. In the top plot of Fig. 1.9 we show the maximal density, ρ_{max} , (light blue, left axis), and the lapse, α , (orange, right axis) as function of time. As can be seen the lapse starts collapsing right after the merger while the maximal density starts to increase dramatically. The collapsing remnant requires a rapid decrease in the numerical time step as described in Sec. 2.5 in [28]. Once the lapse value of a particle decreases below $\alpha_{\text{dust}} = 0.05$, we convert it to "dust", which means that we ignore the particle's internal energy and pressure contribution. This makes the conservative-to-primitive recovery trivial. Below $\alpha_{\text{cut}} = 0.02$ we remove particles from the simulations. As can be double-checked by calculating a posteriori the apparent horizon, this procedure is safe and does not lead to notable artifacts. During the collapse we reach a maximal density of $\rho_{\text{max}} = 5 \times 10^{16} \text{ g/cm}^3$ before the removal of particles kicks in. At the end of the simulation about $7 \times 10^{-4} M_{\odot}$ of material are still outside the black hole out

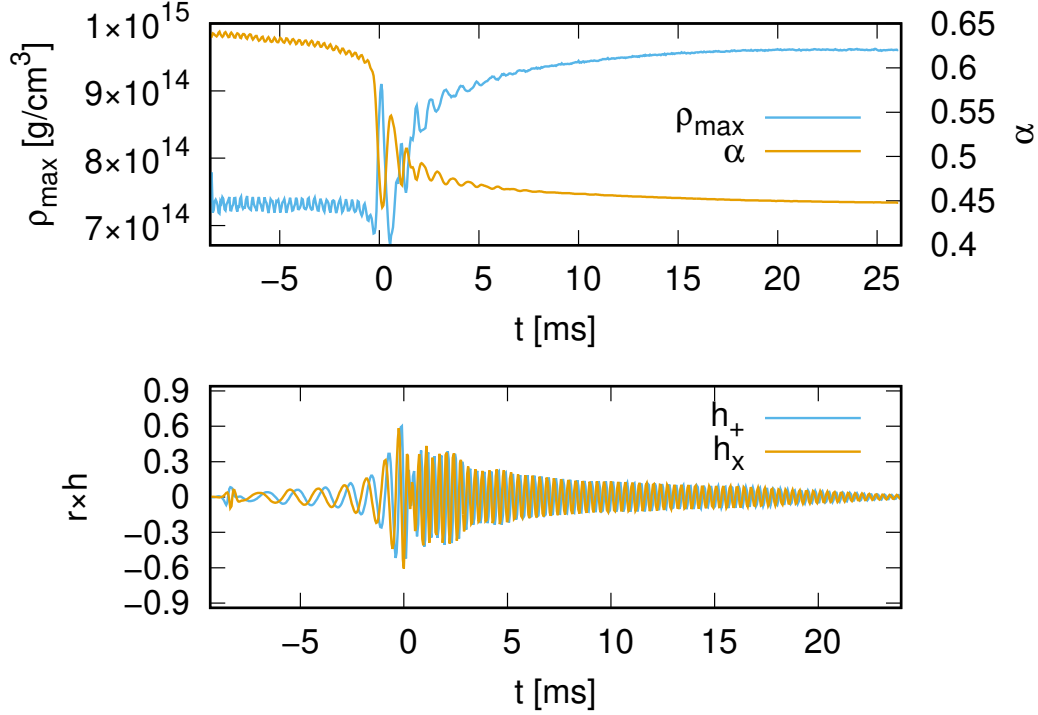


Fig. 1.8: Top: evolution of the peak density and minimum lapse value during the merger of the $2 \times 1.3 M_{\odot}$ merger with APR3 equation of state. Bottom: corresponding gravitational wave amplitudes (multiplied with the distance to the source).

of which about $2 \times 10^{-4} M_{\odot}$ are unbound, and some fraction of which has speeds exceeding $0.7c$. The remaining bound material is expected to fall into the black hole eventually.

In the bottom plot of Fig. 1.9 we show, in light blue, the plus- and, in orange, the cross-polarization of r times the strain extracted from the simulation at an extraction sphere of $R_{\text{extr}} = 150 \approx 221.5$ km. Note that, in both the bottom and the top plot, the data is shifted so that the time of maximal gravitational wave power corresponds to $t = 0$. The waveform initially ($-7 < t < -5.5$ ms) shows some spurious waves from the initial data, but then shows a clean “chirping” inspiral, the merger ($-0.5 < t < 0.6$ ms) and, finally, the black hole ringdown ($t > 0.6$ ms).

We have written a reader for spacetime data for the Einstein Toolkit [86] to analyze the properties of the black hole that forms. We first used `AHFinderDirect` [87, 88] to find the apparent horizon and, once found, `QuasiLocalMeasures` [89, 90] to calculate the spin and total mass of the black holes. The result is shown in Fig. 1.10. Here we show the total mass of the black hole for the 2M particle run in orange, the result of a lower resolution 1M particle run is shown in light blue. As

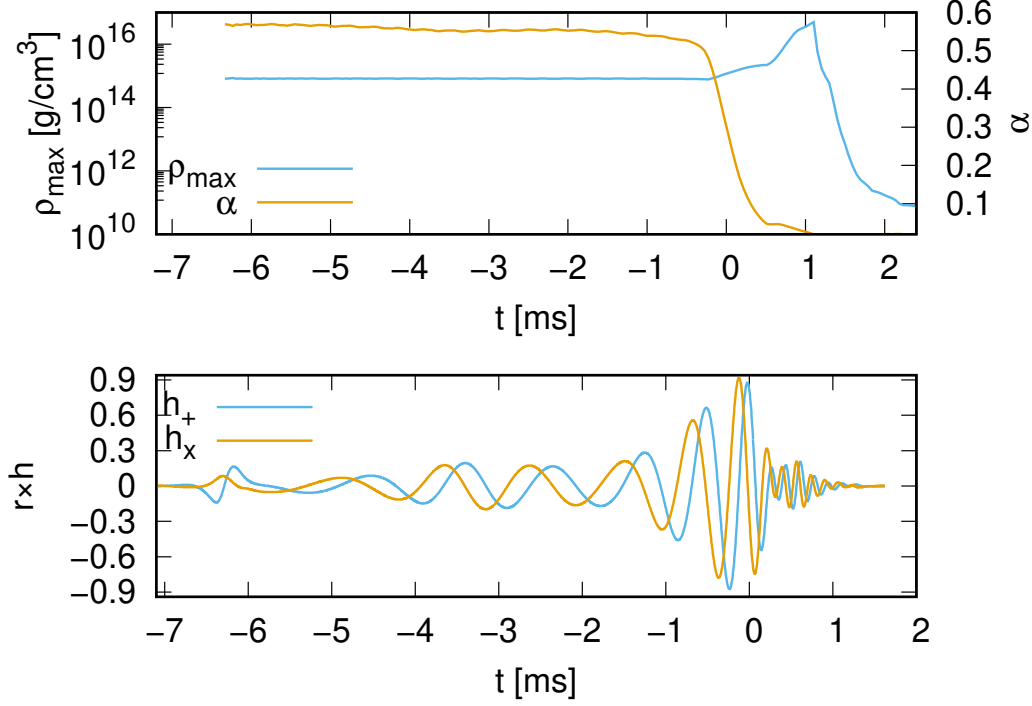


Fig. 1.9: Top plot: we show in blue (left axis) the maximal density, ρ_{\max} , and in orange (right axis) the lapse, α , as function of time for the system with two $1.5 M_{\odot}$ neutron stars with the APR3 equation of state. Bottom plot: we show in blue the plus-polarization, h_+ , and in orange the cross-polarization, h_x , of r times the gravitational wave strain.

can be seen the mass of the black hole grows rapidly at first then slows down and eventually levels off. The dark blue line shows the ADM mass of the initial data, while the black and red lines shows the initial ADM mass¹⁰ minus the energy radiated away in gravitational waves as calculated from the 2M (black) and 1M (red) runs. This is the expected final mass, M_{final} , of the black hole. Both cases produce final black hole masses very close to this value with the 2M run reproducing it to within 0.3 %. For even better agreement, higher resolution would be needed. In the higher resolution run, the final dimensionless spin parameter is $a/M \approx 0.75$.

¹⁰ In General Relativity energy and momentum are non-local quantities and difficult to define since the spacetime itself contributes [91]. There are various definitions of "mass", the ADM mass applies to asymptotically flat spacetimes and can be found by integrating over the spacetime.

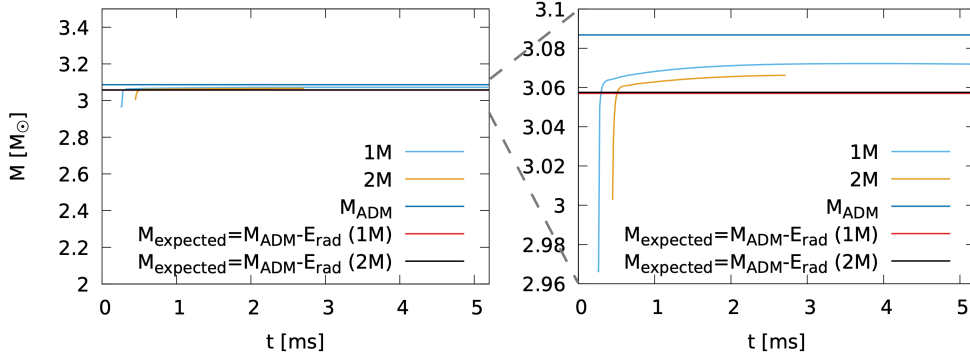


Fig. 1.10: The mass of the black hole (including rotational energy) as function of time (the time has been shifted so zero corresponds to the time of maximal gravitational wave power; left panel is zoom-in of right panel). The orange curve is for the 2M particle runs mentioned earlier, while the light blue curve is for a lower resolution run with 1M particles. The dark blue curve shows the initial ADM mass of the system, while the black and red curves shows the initial ADM mass minus the radiated gravitational wave energy, i.e. the expected final mass of the black hole, as determined by the 2M and 1M runs, respectively.

1.4 Summary and outlook

We have presented here the main methodological elements of the *Lagrangian* numerical relativity code `SPHINCS_BSSN`. This code evolves the spacetime in a very similar fashion to standard *Eulerian* codes, in particular by solving the BSSN equations [17, 18] on an adaptive mesh. The major difference to more conventional numerical relativity codes is that the fluid is evolved by means of Lagrangian particles. This has major advantages for tracking and evolving the matter that is ejected in a neutron star merger. This matter, although only a relatively small fraction ($\sim 1\%$) of the binary mass, is responsible for all the electromagnetic emission and therefore of paramount importance for predicting the multi-messenger signatures on compact binary mergers. This mixed methodology with both particles and adaptive mesh, however, requires an accurate information exchange between the particles and the grid points and this has been one of the major challenges of the development process. As described in Sec. 1.2.3, we have found a way that produces accurate and robust results.

To demonstrate the proper functioning of the hydrodynamic part of `SPHINCS_BSSN` we have performed 3D shock tube tests which show very good agreement with the exact solution and thereby demonstrate the accurate functioning of the hydrodynamic part. Neutron star oscillations where the full spacetime is evolved are a good test for scrutinizing both the spacetime evolution and the coupling of spacetime and hydrodynamics, since measured oscillation frequencies can be compared

against accurately known values from independent approaches. We have evolved a neutron star for ~ 30 ms and measured its oscillation frequencies. We find excellent agreement with the results of [79]: even at low resolution all frequencies agree already to better than 1% and become increasingly more accurate with higher resolution. The neutron star remains essentially perfectly in its initial state and its surface remains very well-behaved without any artifacts. This is a major advantage of SPHINCS_BSSN compared to Eulerian codes. We have further performed two binary neutron star simulations, one where a stable remnant survives and another one where a black hole forms promptly.

After an extensive phase of scrutinizing and further improving our methodology,

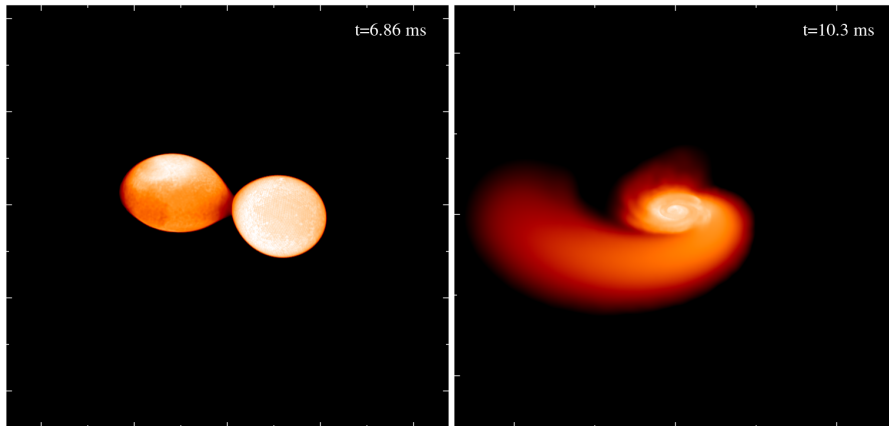


Fig. 1.11: Volume rendering of an equal mass ($2 \times 1.3 M_{\odot}$) binary merger where one of the stars (the left star in the left panel) is rapidly spinning ($\chi_1 = 0.5$) while the other is not ($\chi_2 = 0$). The multi-messenger signatures of such systems are explored in detail in [92].

we have recently begun to simulate astrophysical systems [93]. Fig. 1.11 shows an example of a neutron star binary ($2 \times 1.3 M_{\odot}$, APR3 EOS) where one star is rapidly spinning with dimensionless spin parameter $\chi_1 = 0.5$ while the other star has no spin ($\chi_2 = 0$). Such binaries with only one millisecond neutron star are not just a mere academic possibility, but they likely form in dense stellar environments such as globular clusters via binary-single exchange encounters [92]. The large majority of neutron stars observed in globular clusters are rapidly spinning¹¹ and encounters between a binary, consisting of a spun-up neutron star and a low-mass companion, and another neutron star can easily lead to the exchange of the low mass companion with the neutron star. According to our estimates [92], such binaries may account for approximately $\sim 5\%$ of the merging neutron star systems. Such mergers show a number of distinct signatures in their multi-messenger signals: they dynamically

¹¹ See P. Freire's website https://www3.mpifrbonn.mpg.de/staff/pfreire/NS_masses.html

eject approximately an order of magnitude more matter and therefore produce particularly bright kilonovae. Since the collision itself is less violent they produce a smaller amount of fast ejecta ($> 0.5c$) and therefore weaker blue/UV kilonova precursors [94]. The GW-emission is substantially less efficient and therefore one can expect a longer lived central remnant and one may speculate that such mergers may be related to long GRBs that produce kilonova emission such as GRB 211211A [95] and GRB 230307A [96].

Future development efforts of `SPHINCS_BSSN` include improvements of its parallelization and the implementation of further physics ingredients such as, for example, more realistic nuclear matter equations of state and neutrino transport.

Acknowledgements It is a great pleasure to acknowledge interesting discussions with Sam Toole and we are very grateful for his generous help with the FUKA library. We are further grateful to Kostas Kokkotas and Nick Stergioulas for sharing their insights into oscillating stars and we would also like to thank Diego Calderon, Jan-Erik Christian, Pia Jakobus, Laurens Paulsen, Lukas Schnabel and Wasif Shaquil for their careful reading of an earlier version of this text. SR has been supported by the Swedish Research Council (VR) under grant number 2020-05044, by the research environment grant “Gravitational Radiation and Electromagnetic Astrophysical Transients” (GREAT) funded by the Swedish Research Council (VR) under Dnr 2016-06012, by the Knut and Alice Wallenberg Foundation under grant Dnr. KAW 2019.0112, by the Deutsche Forschungsgemeinschaft (DFG, German Research Foundation) under Germany’s Excellence Strategy - EXC 2121 “Quantum Universe” - 390833306 and by the European Research Council (ERC) Advanced Grant INSPIRATION under the European Union’s Horizon 2020 research and innovation programme (Grant agreement No. 101053985).

Parts of the simulations for this chapter have been performed on the facilities of North-German Supercomputing Alliance (HLRN), and at the SUNRISE HPC facility supported by the Technical Division at the Department of Physics, Stockholm University. Special thanks go to Holger Motzkau and Mikica Kocic for their excellent support in upgrading and maintaining SUNRISE. Portions of this research were conducted with high performance computing resources provided by Louisiana State University (<http://www.hpc.lsu.edu>).

References

- [1] A. Einstein, Sitzungsberichte der Königlich Preußischen Akademie der Wissenschaften (Berlin), Seite 688-696. , 688 (1916).
- [2] A. Einstein, Sitzungsberichte der Königlich Preußischen Akademie der Wissenschaften (Berlin), Seite 154-167. , 154 (1918).
- [3] D. Kennefick, *Traveling at the Speed of Thought: Einstein and the Quest for Gravitational Waves* (2007).
- [4] R. A. Hulse and J. H. Taylor, *ApJL* **195**, L51 (1975).
- [5] B. P. Abbott, R. Abbott, T. D. Abbott, M. R. Abernathy, F. Acernese, K. Ackley, C. Adams, T. Adams, P. Addesso, R. X. Adhikari, and et al., *Physical Review Letters* **116**, 061102 (2016), [arXiv:1602.03837 \[gr-qc\]](https://arxiv.org/abs/1602.03837) .
- [6] R. Margutti and R. Chornock, *Ann. Rev. of Astronomy and Astrophysics* **59**, 155 (2021), [arXiv:2012.04810 \[astro-ph.HE\]](https://arxiv.org/abs/2012.04810) .

- [7] A. J. Levan, J. D. Lyman, N. R. Tanvir, J. Hjorth, I. Mandel, E. R. Stanway, D. Steeghs, A. S. Fruchter, E. Troja, S. L. Schröder, and K. e. a. Wiersema, *ApJL* **848**, L28 (2017), [arXiv:1710.05444 \[astro-ph.HE\]](#) .
- [8] B. P. Abbott, R. Abbott, T. D. Abbott, F. Acernese, K. Ackley, C. Adams, T. Adams, P. Addesso, R. X. Adhikari, V. B. Adya, and et al., *ApJL* **848**, L13 (2017), [arXiv:1710.05834 \[astro-ph.HE\]](#) .
- [9] B. P. Abbott, R. Abbott, T. D. Abbott, F. Acernese, K. Ackley, C. Adams, T. Adams, P. Addesso, R. X. Adhikari, V. B. Adya, and et al., *ApJL* **848**, L12 (2017), [arXiv:1710.05833 \[astro-ph.HE\]](#) .
- [10] J. M. Lattimer, F. Mackie, D. G. Ravenhall, and D. N. Schramm, *ApJ* **213**, 225 (1977).
- [11] E. Symbalisty and D. N. Schramm, *Astrophys. Lett.* **22**, 143 (1982).
- [12] D. Eichler, M. Livio, T. Piran, and D. N. Schramm, *Nature* **340**, 126 (1989).
- [13] S. Rosswog, M. Liebendörfer, F.-K. Thielemann, M. Davies, W. Benz, and T. Piran, *A & A* **341**, 499 (1999).
- [14] C. Freiburghaus, S. Rosswog, and F.-K. Thielemann, *ApJ* **525**, L121 (1999).
- [15] J. J. Cowan, C. Sneden, J. E. Lawler, A. Aprahamian, M. Wiescher, K. Langanke, G. Martinez-Pinedo, and F.-K. Thielemann, *Reviews of Modern Physics* **93**, 015002 (2021), [arXiv:1901.01410 \[astro-ph.HE\]](#) .
- [16] B. P. Abbott, R. Abbott, T. D. Abbott, F. Acernese, K. Ackley, C. Adams, T. Adams, P. Addesso, R. X. Adhikari, V. B. Adya, and et al., *Nature* **551**, 85 (2017), [arXiv:1710.05835](#) .
- [17] M. Alcubierre, *Introduction to 3+1 Numerical Relativity* (Oxford University Press, 2008).
- [18] T. W. Baumgarte and S. L. Shapiro, *Numerical Relativity: Solving Einstein's Equations on the Computer*, edited by Baumgarte, T. W. & Shapiro, S. L. (Cambridge University Press, ISBN: 9780521514071, Cambridge, 2010).
- [19] L. Rezzolla and O. Zanotti, *Relativistic Hydrodynamics* (Oxford University Press, 2013. ISBN-10: 0198528906; ISBN-13: 978-0198528906, 2013).
- [20] M. Shibata, *Numerical Relativity* (World Scientific, 2016).
- [21] A. Mezzacappa, E. Endeve, O. E. B. Messer, and S. W. Bruenn, *Living Reviews in Computational Astrophysics* **6**, 4 (2020), [arXiv:2010.09013 \[astro-ph.HE\]](#) .
- [22] D. Radice, S. Bernuzzi, A. Perego, and R. Haas, *MNRAS* (2022), [10.1093/mnras/stac589](#), [arXiv:2111.14858 \[astro-ph.HE\]](#) .
- [23] F. Foucart, *Living Reviews in Computational Astrophysics* **9**, 1 (2023), [arXiv:2209.02538 \[astro-ph.HE\]](#) .
- [24] W. H. Press, B. P. Flannery, S. A. Teukolsky, and W. T. Vetterling, *Numerical Recipes* (Cambridge University Press, New York, 1992).
- [25] S. Rosswog and P. Diener, *Classical and Quantum Gravity* **38**, 115002 (2021), [arXiv:2012.13954 \[gr-qc\]](#) .
- [26] P. Diener, S. Rosswog, and F. Torsello, *European Physical Journal A* **58**, 74 (2022), [arXiv:2203.06478 \[astro-ph.HE\]](#) .
- [27] S. Rosswog, P. Diener, and F. Torsello, *Symmetry* **14**, 1280 (2022), [arXiv:2205.08130 \[gr-qc\]](#) .

- [28] S. Rosswog, F. Torsello, and P. Diener, *Front. Appl. Math. Stat.* **9** (2023), [10.48550/arXiv.2306.06226](https://doi.org/10.48550/arXiv.2306.06226), [arXiv:2306.06226 \[gr-qc\]](https://arxiv.org/abs/2306.06226) .
- [29] J. J. Monaghan, *Ann. Rev. Astron. Astrophys.* **30**, 543 (1992).
- [30] J. J. Monaghan, *Reports on Progress in Physics* **68**, 1703 (2005).
- [31] S. Rosswog, *New Astronomy Reviews* **53**, 78 (2009).
- [32] V. Springel, *ARAA* **48**, 391 (2010), [arXiv:1109.2219 \[astro-ph.CO\]](https://arxiv.org/abs/1109.2219) .
- [33] D. J. Price, *Journal of Computational Physics* **231**, 759 (2012), [arXiv:1012.1885 \[astro-ph.IM\]](https://arxiv.org/abs/1012.1885) .
- [34] S. Rosswog, *MNRAS* **448**, 3628 (2015), [arXiv:1405.6034 \[astro-ph.IM\]](https://arxiv.org/abs/1405.6034) .
- [35] S. Rosswog, *Living Reviews of Computational Astrophysics* (2015) **1** (2015), [10.1007/lrca-2015-1](https://doi.org/10.1007/lrca-2015-1), [arXiv:1406.4224 \[astro-ph.IM\]](https://arxiv.org/abs/1406.4224) .
- [36] P. Laguna, W. A. Miller, and W. H. Zurek, *ApJ* **404**, 678 (1993).
- [37] S. Siegler and H. Riffert, *ApJ* **531**, 1053 (2000), [arXiv:astro-ph/9904070](https://arxiv.org/abs/astro-ph/9904070) .
- [38] J. J. Monaghan and D. J. Price, *MNRAS* **328**, 381 (2001).
- [39] S. Rosswog, *Classical and Quantum Gravity* **27**, 114108 (2010).
- [40] S. Rosswog, *J. Comp. Phys.* **229**, 8591 (2010), [arXiv:0907.4890](https://arxiv.org/abs/0907.4890) .
- [41] S. Rosswog, *Springer Lecture Notes in Computational Science and Engineering*, "Meshfree Methods for Partial Differential Equations V", Eds. M. Griebel, M.A. Schweitzer, Heidelberg, p. 89-103 (2011).
- [42] V. Springel, *MNRAS* **401**, 791 (2010), [arXiv:0901.4107 \[astro-ph.CO\]](https://arxiv.org/abs/0901.4107) .
- [43] P. C. Duffell and A. I. MacFadyen, *ApJS* **197**, 15 (2011), [arXiv:1104.3562 \[astro-ph.HE\]](https://arxiv.org/abs/1104.3562) .
- [44] P. F. Hopkins, *MNRAS* **428**, 2840 (2013), [arXiv:1206.5006 \[astro-ph.IM\]](https://arxiv.org/abs/1206.5006) .
- [45] R. M. Cabezón, D. García-Senz, and J. Figueira, *A & A* **606**, A78 (2017), [arXiv:1607.01698 \[astro-ph.IM\]](https://arxiv.org/abs/1607.01698) .
- [46] J. J. Monaghan, *Journal of Computational Physics* **60**, 253 (1985).
- [47] V. Springel and L. Hernquist, *MNRAS* **333**, 649 (2002).
- [48] J. J. Monaghan, *MNRAS* **335**, 843 (2002).
- [49] S. Rosswog and D. Price, *MNRAS* **379**, 915 (2007).
- [50] R. A. Gingold and J. J. Monaghan, *Journal of Computational Physics* **46**, 429 (1982).
- [51] R. Speith, *Untersuchung von Smoothed Particle Hydrodynamics anhand astrophysikalischer Beispiele*, Ph.D. thesis, Eberhard-Karls-Universität Tübingen (1998).
- [52] D. Price and J. Monaghan, *MNRAS* **374**, 1347 (2007).
- [53] V. Fock, *Theory of Space, Time and Gravitation* (Pergamon, Oxford, 1964).
- [54] B. Schutz, *A first course in general relativity*, 1st ed. (Cambridge University Press, Cambridge, 1989).
- [55] S.-I. Inutsuka, *Journal of Computational Physics* **179**, 238 (2002), [arXiv:astro-ph/0206401](https://arxiv.org/abs/astro-ph/0206401) .
- [56] E. Toro, *Riemann Solvers and Numerical Methods for Fluid Dynamics* (Springer, Berlin, 1999).
- [57] S. Rosswog, *MNRAS* **498**, 4230 (2020), [arXiv:1911.13093 \[astro-ph.IM\]](https://arxiv.org/abs/1911.13093) .
- [58] J. von Neumann and R. D. Richtmyer, *Journal of Applied Physics* **21**, 232 (1950).

- [59] L. Cullen and W. Dehnen, *MNRAS* **408**, 669 (2010), [arXiv:1006.1524 \[astro-ph.IM\]](#) .
- [60] J.-L. Guermond, R. Pasquetti, and B. Popov, *Journal of Computational Physics* **230**, 4248 (2011).
- [61] J.-L. Guermond, B. Popov, and V. Tomov, *Computer Methods in Applied Mechanics and Engineering* **300**, 402 (2016).
- [62] S. Rosswog, *ApJ* **898**, 60 (2020), [arXiv:1912.01095 \[astro-ph.IM\]](#) .
- [63] M. Cernetic, V. Springel, T. Guillet, and R. Pakmor, *MNRAS* **522**, 982 (2023), [arXiv:2208.11131 \[astro-ph.IM\]](#) .
- [64] M. Caldana, P. F. Antonietti, and L. Dede', *arXiv e-prints* , [arXiv:2402.16517 \(2024\)](#), [arXiv:2402.16517 \[math.NA\]](#) .
- [65] J. J. Monaghan, *Journal of Computational Physics* **136**, 298 (1997).
- [66] D. Balsara, *J. Comput. Phys.* **121**, 357 (1995).
- [67] J. Morris and J. Monaghan, *J. Comp. Phys.* **136**, 41 (1997).
- [68] P. L. Roe, *Annual Review of Fluid Mechanics* **18**, 337 (1986).
- [69] J. W. York, in *Sources of Gravitational radiation*, edited by L. L. Smarr (Cambridge University Press, Cambridge, UK, 1979) pp. 83–126.
- [70] R. Arnowitt, S. Deser, and C. W. Misner, in *Gravitation: An Introduction to Current Research*, edited by L. Witten (Wiley, New York, 1962) pp. 227–265.
- [71] F. X. Timmes and F. D. Swesty, *ApJS* **126**, 501 (2000).
- [72] G.-H. Cottet and P. D. Koumoutsakos, *Vortex Methods* (2000).
- [73] S. Diot, R. Loubere, and S. Clain, *International Journal for Numerical Methods in Fluids* **73**, 362 (2013).
- [74] G. Sod, *J. Comput. Phys.* **43**, 1 (1978).
- [75] J. Marti and E. Müller, *J. Comp. Phys.* **123**, 1 (1996).
- [76] J. E. Chow and J. Monaghan, *J. Computat. Phys.* **134**, 296 (1997).
- [77] L. Del Zanna and N. Bucciantini, *A&A* **390**, 1177 (2002), [arXiv:astro-ph/0205290](#) .
- [78] J. M. Marti and E. Müller, *Living Reviews in Relativity* **6**, 7 (2003).
- [79] J. A. Font, T. Goodale, S. Iyer, M. Miller, L. Rezzolla, E. Seidel, N. Stergioulas, W.-M. Suen, and M. Tobias, *Phys. Rev. D* **65**, 084024 (2002).
- [80] R. C. Tolman, *Physical Review* **55**, 364 (1939).
- [81] J. R. Oppenheimer and G. M. Volkoff, *Physical Review* **55**, 374 (1939).
- [82] J. S. Read, B. D. Lackey, B. J. Owen, and J. L. Friedman, *Phys. Rev. D* **79**, 124032 (2009), [arXiv:0812.2163 \[astro-ph\]](#) .
- [83] A. Akmal, V. R. Pandharipande, and D. G. Ravenhall, *Phys. Rev. C* **58**, 1804 (1998), [hep-ph/9804388](#) .
- [84] L. J. Papenfort, S. D. Tootle, P. Grandclément, E. R. Most, and L. Rezzolla, *Phys. Rev. D* **104**, 024057 (2021), [arXiv:2103.09911 \[gr-qc\]](#) .
- [85] G. Bozzola, *The Journal of Open Source Software* **6**, 3099 (2021), [arXiv:2104.06376 \[gr-qc\]](#) .
- [86] F. Löffler, J. Faber, E. Bentivegna, T. Bode, P. Diener, R. Haas, I. Hinder, B. C. Mundim, C. D. Ott, E. Schnetter, G. Allen, M. Campanelli, and P. Laguna, *Classical and Quantum Gravity* **29**, 115001 (2012), [arXiv:1111.3344 \[gr-qc\]](#) .
- [87] J. Thornburg, *Phys. Rev. D* **54**, 4899 (1996), [gr-qc/9508014](#) .

- [88] J. Thornburg, *Class. Quantum Grav.* **21**, 743 (2004), [gr-qc/0306056](#) .
- [89] O. Dreyer, B. Krishnan, D. Shoemaker, and E. Schnetter, *Phys. Rev. D* **67**, 024018 (2003), [arXiv:gr-qc/0206008](#) .
- [90] E. Schnetter, B. Krishnan, and F. Beyer, *Phys. Rev. D* **74**, 024028 (2006), [arXiv:gr-qc/0604015](#) .
- [91] C. Misner, K. Thorne, and J. Wheeler, *Gravitation* (Freeman, New York, 1973).
- [92] S. Rosswog, P. Diener, F. Torsello, T. Tauris, and N. Sarin, [arXiv e-prints](#) , [arXiv:2310.15920](#) (2023), [arXiv:2310.15920 \[astro-ph.HE\]](#) .
- [93] S. Rosswog and O. Korobkin, *Annalen der Physik* **536**, 2200306 (2024), [arXiv:2208.14026 \[astro-ph.HE\]](#) .
- [94] B. D. Metzger, A. Bauswein, S. Goriely, and D. Kasen, *MNRAS* **446**, 1115 (2015), [arXiv:1409.0544 \[astro-ph.HE\]](#) .
- [95] J. C. Rastinejad, B. P. Gompertz, A. J. Levan, W.-f. Fong, M. Nicholl, G. P. Lamb, D. B. Malesani, A. E. Nugent, and more, *Nature* **612**, 223 (2022), [arXiv:2204.10864 \[astro-ph.HE\]](#) .
- [96] A. J. Levan, B. P. Gompertz, O. S. Salafia, M. Bulla, E. Burns, K. Hotokezaka, L. Izzo, G. P. Lamb, D. B. Malesani, S. R. Oates, M. E. Ravasio, A. Rouco Escorial, B. Schneider, N. Sarin, S. Schulze, N. R. Tanvir, K. Ackley, G. Anderson, G. B. Brammer, L. Christensen, V. S. Dhillon, P. A. Evans, M. Fausnaugh, W.-f. Fong, A. S. Fruchter, C. Fryer, J. P. U. Fynbo, N. Gaspari, K. E. Heintz, J. Hjorth, J. A. Kennea, M. R. Kennedy, T. Laskar, G. Leloudas, I. Mandel, A. Martin-Carrillo, B. D. Metzger, M. Nicholl, A. Nugent, J. T. Palmerio, G. Pugliese, J. Rastinejad, L. Rhodes, A. Rossi, A. Saccardi, S. J. Smartt, H. F. Stevance, A. Tohuvavohu, A. van der Horst, S. D. Vergani, D. Watson, T. Barclay, K. Bhirombhakdi, E. Breedt, A. A. Breeveld, A. J. Brown, S. Campana, A. A. Chrimes, P. D'Avanzo, V. D'Elia, M. De Pasquale, M. J. Dyer, D. K. Galloway, J. A. Garbutt, M. J. Green, D. H. Hartmann, P. Jakobsson, P. Kerry, C. Kouveliotou, D. Langeroodi, E. Le Floc'h, J. K. Leung, S. P. Littlefair, J. Munday, P. O'Brien, S. G. Parsons, I. Pelisoli, D. I. Sahman, R. Salvaterra, B. Sbarufatti, D. Steeghs, G. Tagliaferri, C. C. Thöne, A. de Ugarte Postigo, and D. A. Kann, *Nature* **626**, 737 (2024), [arXiv:2307.02098 \[astro-ph.HE\]](#) .